STEM CELLS

DLX2 acts as a pioneer factor and drives *Msx1*$^+$ ectomesenchyme formation from embryonic stem cells

Ziwei Zhang[1,2]†, Zhiheng Xu[1]†, Hong Hu[1,3]†, Yao Li[4]†, Youmei Jin[5], Yi Zhong[5], Yunqiu Zhang[1,2], Yike Yin[1], Jing Chen[4]*, Yufeng Duan[6]*, Hao Yang[5]*, Zhonghan Li[1,2,7]*

The ectomesenchyme generates much of the craniofacial skeleton, sutures, and diverse connective tissues in the mammalian head, yet its derivation from embryonic stem cells (ESCs) and the underlying molecular drivers remain poorly defined. Here, we identified *Dlx2* as a key regulator that efficiently directed murine ESCs toward *Msx1*$^+$ ectomesenchyme, recapitulating the developmental trajectory. These *Msx1*$^+$ progenitors expressed classical craniofacial markers, exhibited robust osteochondral differentiation potential as a group, and supported craniofacial regeneration. Mechanistically, Distal-less homeobox 2 (DLX2) formed a complex with lamina-associated polypeptide 2, isoform alpha (LAP2α) through a 38–amino-acid homeodomain motif, interacting with nucleosomes to promote chromatin remodeling and activate a procraniofacial ectomesenchymal gene network. Disrupting DLX2-LAP2α interaction or silencing *Dlx2* targets markedly diminished ectomesenchymal differentiation. Our findings established DLX2 as a pioneer factor in ectomesenchyme specification, offering insights into craniofacial development and stem cell engineering.

INTRODUCTION

The ectomesenchyme gives rise to a series of tissues in mammalian head, including much of the craniofacial skeleton, suture, and connective tissues, and plays critical roles in proper patterning of facial muscular, vascular, and neural tissues (*1*–*3*). Deficiency in ectomesenchyme often has dire consequences on human embryonic development (*2*). For example, meninges are a direct derivative of ectomesenchyme, and their abnormality may cause Dandy-Walker malformation, a rare and serious congenital disease with hypoplasia of the cerebellum (*4*). Other craniofacial dysmorphia includes craniosynostosis, or Saethre-Chotzen syndrome, a disease marked by premature fusion of the suture, which affects calvaria expansion during brain development (*5*), and cleft lip and palate, one of the most common congenital craniofacial abnormalities (*6*). Recent findings indicated that transplantation of primary craniofacial mesenchymal stem cells promoted suture regeneration and sustained calvaria development (*7*). Thus, derivation of ectomesenchymal progenitors may hold promises in both basic developmental biology and potential translational use in reversing craniofacial abnormalities.

Developmentally, ectomesenchyme is a major derivative of cranial neural crest, a transient population of multipotent stem cells that undergo extensive epithelial-to-mesenchymal transition (EMT) and migration (*8*). When cranial neural crest cells (CNCCs) migrate into the craniofacial regions, they further differentiate into ectomesenchyme that gives rise to craniofacial skeleton, suture, and connective tissues and nonectomesenchyme that generates neurons, glia, and pigment cells (*8*). The differentiation of CNCCs from pluripotent stem cells has been readily achieved through combining multiple signaling cues, such as Wnt, bone morphogenetic protein (BMP), and fibroblast growth factor (FGF) modulation to mimic the developmental process (*9*–*12*). Significant challenges remain in generating ectomesenchymal progenitors from CNCCs. Current CNCC-derived mesenchymal stromal cells (MSCs) expressed common mesenchymal markers (e.g., CD73, CD105, and CD146) (*13*–*15*) but lacked specific functional or molecular characterization to confirm their ectomesenchymal identity and distinguish them from mesoderm-derived MSCs. Therefore, the actual lineage identity of CNCC-derived ectomesenchymal progenitors was not defined, and how pluripotent stem cells could be directly induced into bona fide ectomesenchyme remains elusive.

The highly conserved *Dlx* (Distal-less homeobox) gene family plays pivotal roles in craniofacial development, orchestrating the patterning and differentiation of craniofacial ectomesenchyme and forebrain morphogenesis (*16*). During embryogenesis, *Dlx* genes exhibit nested and overlapping expression patterns along the pharyngeal arches (PAs) and within the cranial neural crest, where they critically regulate the patterning, differentiation, and morphogenesis of ectomesenchymal derivatives, including bone, cartilage, and teeth, to ensure proper facial structure formation (*2*, *17*). Despite functional redundancies among *Dlx* genes, their knockout (KO) in mice frequently results in craniofacial malformations (*2*). However, whether *Dlx* genes are sufficient to drive ectomesenchymal fate specification all the way from embryonic stem cells (ESCs) and the molecular mechanisms underlying their nuclear regulatory functions remains poorly understood, warranting further investigation.

[1]Center of Growth Metabolism and Aging, Key Laboratory of Bio-Resource and Eco-Environment of Ministry of Education, Animal Disease Prevention and Food Safety Key Laboratory of Sichuan Province, College of Life Sciences, Sichuan University, Chengdu 610065, China. [2]Frontiers Medical Center, Tianfu Jincheng Laboratory, Chengdu 610041, China. [3]College of Basic Medical Sciences and Forensic Medicine, Henan University of Science and Technology, Luoyang 471023, China. [4]Department of Pediatric Surgery and Laboratory of Pediatric Surgery, West China Hospital, Sichuan University, Chengdu 610041, China. [5]Liver Surgery and NHC Key Lab of Transplant Engineering and Immunology, Proteomics-Metabolomics Platform of Core Facilities, West China Hospital, Sichuan University, Chengdu 610041, China. [6]Department of Orthodontics, Shanghai Ninth People's Hospital, Shanghai Jiao Tong University School of Medicine; College of Stomatology, Shanghai Jiao Tong University; National Center for Stomatology; National Clinical Research Center for Oral Diseases; Shanghai Key Laboratory of Stomatology; Shanghai Research Institute of Stomatology, Shanghai 200011, China. [7]Yunnan Key Laboratory of Stomatology, Department of Pediatric Dentistry, The Affiliated Stomatology Hospital of Kunming Medical University, Kunming Medical University, Kunming 650500, China.
*Corresponding author. Email: zhonghan.li@outlook.com (Z.L.); yanghao@scu.edu.cn (H.Y.); dyfican@163.com (Y.D.); jingchen@scu.edu.cn (J.C.)
†These authors contributed equally to this work.

In this study, we used a previously established Msx1:P2A-tdTomato (hereafter referred as *Msx1*-tdTomato) reporter knock-in mouse model (*18*), where strong tdTomato (tdT) expression was also detected in the PAs and facial prominences during embryogenesis. A targeted inducible screen of transcriptional factors was then carried out in *Msx1*-tdTomato ESCs and identified *Dlx2* as a key driver to induce *Msx1*$^+$ ectomesenchymal differentiation. *Dlx2*-induced *Msx1*$^+$ ectomesenchymal progenitors expressed classical craniofacial mesenchymal markers, exhibited strong osteochondral differentiation potential as a group, and contributed to craniofacial bone repair. Mechanistically, DLX2 formed a complex with lamina-associated polypeptide 2, isoform alpha (LAP2α) and nucleosomes via a 38–amino-acid homeodomain motif to regulate ectomesenchymal gene expression. Disrupting DLX2-LAP2α interaction or silencing *Dlx2* targets largely diminished ectomesenchymal differentiation. Thus, our work uncovered DLX2 as a pioneer factor in driving ectomesenchyme lineage specification from ESCs, providing a foundation for advancing craniofacial development and regenerative therapies.

RESULTS

Msx1 marked ectomesenchyme in facial prominences

Previously, we constructed a *Msx1*-tdTomato reporter mouse for tracking dental mesenchyme development, where a P2A-tdTomato cassette was inserted downstream of *Msx1* CDS (*18*). When examining the reporter expression at different developmental stages, tdT was specifically expressed in both facial prominence and limb bud mesenchyme from embryonic day 10.5 (E10.5) to E14.5 (Fig. 1, A and B). At E10.5, *Msx1* expression was predominantly detected in the maxillary, mandibular, and frontonasal prominences. By E12.5 and E14.5, *Msx1* was predominantly expressed in the anterior regions of the maxillary and mandibular prominences and remained detectable in the medial and lateral nasal prominences. Flow cytometry analysis confirmed that about 60 to 80% of cells in facial prominences were tdT$^+$ at these stages (Fig. 1, C and D). To identify signature genes that distinguished craniofacial versus limb bud *Msx1*$^+$ progenitors, we first reanalyzed the transcriptome data of craniofacial and limb tissues from the published database (*19*) and characterized a panel of craniofacial or limb-specific genes, including *Barx1*, *Lhx6/8*, *Dlx1/2*, and *Foxf1/2* for craniofacial markers while *Hoxa9-11*, *Hoxd10/11*, and *Lhx9* for limb bud mesenchyme (Fig. 1E). These signature genes were then further evaluated in *Msx1*$^+$ cells from primary facial prominences and limb bud tissues. Among them, *Dlx1*, *Lhx8*, *Foxf1*, and *Barx1*, but not *Msx1* and *Prrx1*, were indeed only highly enriched in the facial prominence cells, suggesting that they were bona fide craniofacial mesenchymal markers (Fig. 1F). Together, these data supported that during mouse embryogenesis, *Msx1* could mark a group of ectomesenchymal progenitors in facial prominences, which were highly enriched with craniofacial signature genes, including *Dlx1*, *Lhx8*, *Foxf1*, and *Barx1*.

Dlx2 as a key driver of *Msx1*$^+$ ectomesenchymal specification from mESCs

To identify key factors that could drive ectomesenchymal differentiation, we focused on transcription factors (TFs), which play central roles in determining cell lineage identity (*20*). A short list of TFs with documented craniofacial phenotypes in KO animals was selected, including *Msx1* (*21*, *22*), *Pax9* (*23*), *Dlx2* (*24*), *Barx1* (*25*), *Lef1* (*26*, *27*), *Lhx8* (*28*), and *Prrx2* (*29*). These TFs were cloned into an all-in-one PiggyBac (PB) transposon–based doxycycline (Dox)–inducible expression system (fig. S1A), where a control vector expressing only green fluorescent protein (GFP) was also constructed for comparison. The inducible expression of GFP and cloned TFs were validated using flow cytometry analysis and reverse transcription quantitative polymerase chain reaction (RT-qPCR) (fig. S1, B and C). The nuclear localization of representative TFs, where commercial antibodies were available, was also confirmed by immunostaining (fig. S1D).

To test whether the expression of selected TFs could induce ectomesenchymal differentiation, we transfected the Dox-inducible TFs into the *Msx1*-tdTomato murine ESCs (mESCs) to generate stable overexpression (OE) cells first, and the OE cells were then differentiated through the classical embryoid body (EB) method before flow cytometry and RT-qPCR analysis (Fig. 2A). At day 8 of EB induction, using undifferentiated mESCs as the negative control, flow cytometry and statistical analyses of multiple differentiation batches indicated that only *Prrx2* and *Dlx2*-OE induced a statistically substantial increased derivation of tdT$^+$ cells compared with the GFP-OE control (Fig. 2, B and C). Using previously identified craniofacial signature genes (Fig. 1E), RT-qPCR analysis revealed that only *Dlx2*-OE resulted in broad induction of craniofacial markers (Fig. 2D and fig. S1E). Thus, *Dlx2*-OE cells were used for further characterization.

To confirm that ectomesenchymal differentiation occurred specially within the *Msx1*$^+$ population under *Dlx2* OE, we sorted EBs from *Dlx2*-inducible mESCs cultured with or without Dox into *Msx1*$^+$ and *Msx1*$^-$ populations by fluorescence-activated cell sorting (FACS) and analyzed for selected marker expression by RT-qPCR. *Msx1*$^+$ cells sorted from uninduced EBs exhibited high levels of the mesoderm markers *Brachyury* (*T*) and *Mixl1*, indicating spontaneous differentiation toward the mesoderm lineage in the absence of *Dlx2* induction (Fig. 2E). On the other hand, *Msx1*$^+$ cells sorted from the *Dlx2*-OE group exhibited strong induction of ectoderm/neural crest markers such as *Ngfr* (*p75*) and *Tfap2a*, supporting their ectodermal lineage (Fig. 2E). Further analysis indicated that *Dlx2*-OE *Msx1*$^+$ cells were highly enriched with craniofacial signature markers, including *Msx1*, *Prrx1*, *Lhx8*, *Barx1*, *Dlx5*, and *Pax9*, and more general mesenchymal markers such as *Twist1* and *Hand2*, and they became more mature after sustained induction of *Dlx2* (day 16) (Fig. 2F). To validate the key role of *Dlx2* in ectomesenchymal differentiation, we knocked down *Dlx2* using short hairpin RNAs (shRNAs) in spontaneously differentiated EBs (fig. S2, A and B). Although we did not observe significant changes in the percentage of *Msx1*$^+$ cells (fig. S2C), *Dlx2* knockdown (KD) led to a marked decrease in the expression of ectomesenchyme-related marker genes, including *Barx1*, *Lhx8*, *Dlx1*, and *Foxf1*. In addition, the expressions of *Msx1* and *Prrx1* were also reduced (fig. S2D). To investigate whether *Dlx2*-OE would cause craniofacial phenotype in vivo, we also constructed a heat-inducible *dlx2a* OE system in zebrafish (fig. S3A). Heat-shock induction of *dlx2a* expression indeed resulted in strong phenotypes (fig. S3, B and C), and RT-qPCR analysis further confirmed the aberrant induction of craniofacial genes in these zebrafish (fig. S3D). Meanwhile, endodermal markers (*foxa2* and *sox17*) and mesodermal markers (*ndrl*, *mixl1*, and *tbxta*) were either slightly down-regulated or unchanged (fig. S3E). Collectively, these findings demonstrate that *Dlx2* OE directly drives lineage specification of *Msx1*$^+$ ectomesenchyme from mESCs in vitro and

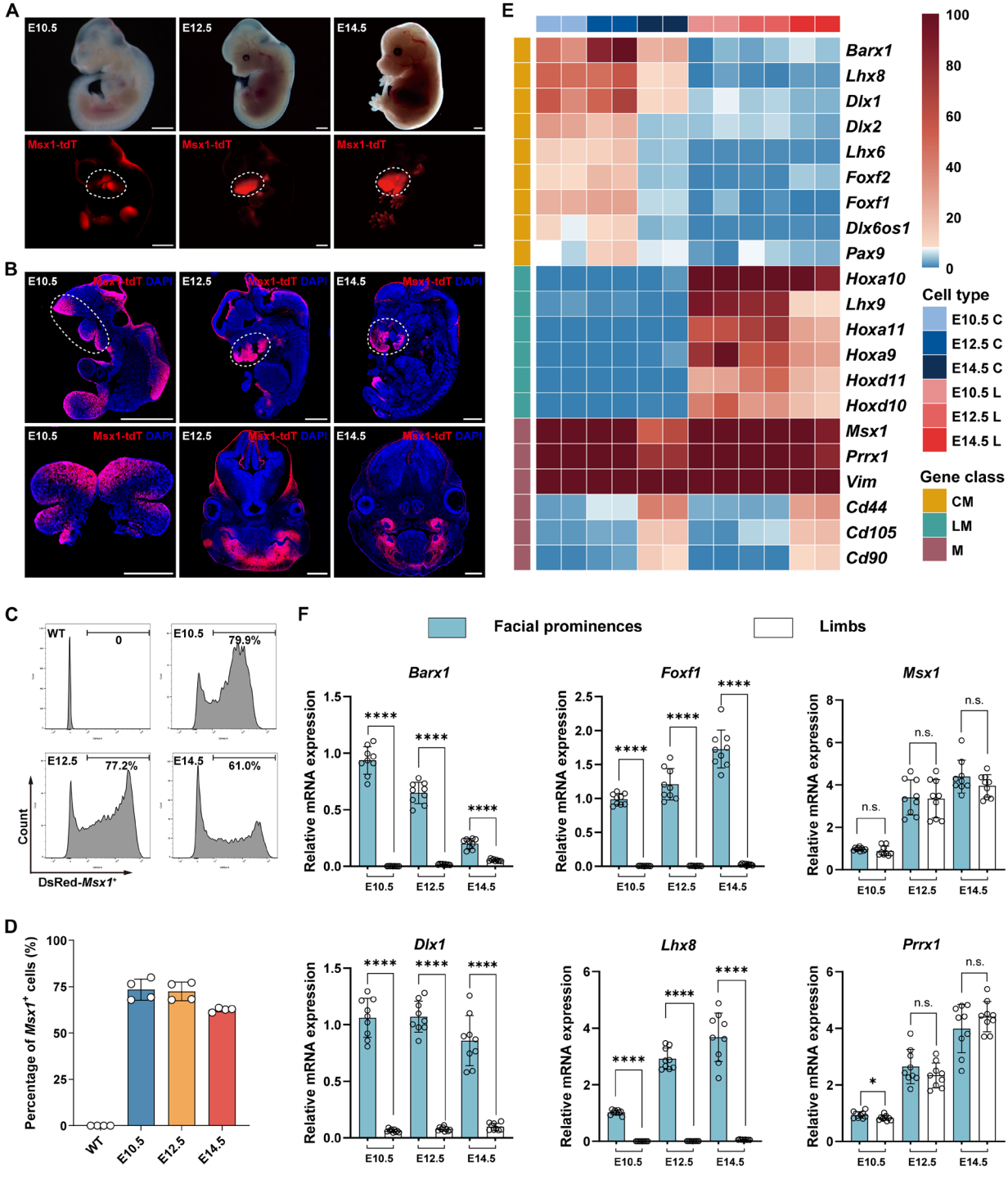

Fig. 1. Expression pattern of *Msx1* in facial prominences and limb mesenchyme. (**A**) Representative fluorescent images of developing embryos (E10.5 to E14.5) from Msx1$^{P2A\text{-}tdTomato}$ reporter mice showing tdT expression in the facial prominences and limbs. Scale bars, 1 mm. (**B**) Immunostaining detection of tdT expression in the facial prominence region. DAPI (4′,6-diamidino-2-phenylindole) was used for nuclear staining. Scale bars, 1 mm. (**C**) Flow cytometry analysis of *Msx1*$^+$ mesenchymal (tdT$^+$) cells in dissociated primary facial prominence tissues. Wild-type (WT) cells were used as the negative control. (**D**) Quantitative analysis of *Msx1*$^+$ cells within the facial prominence regions. Error bars represented data as mean ± SD from two independent experiments with duplicates. (**E**) Heatmap of gene expression in craniofacial and limb regions generated from reanalysis of publicly available bulk RNA sequencing (RNA-seq) datasets (*19*), showing region-specific gene enrichment. C, craniofacial; L, limb; CM, craniofacial mesenchyme; LM, limb mesenchyme; M, mesenchyme. (**F**) Reverse transcription quantitative polymerase chain reaction (RT-qPCR) analysis of selected craniofacial-enriched and general mesenchymal markers in *Msx1*$^+$ cells sorted from facial prominence and limb tissues. Facial prominence markers: *Barx1*, *Foxf1*, *Dlx1*, and *Lhx8*; general mesenchymal markers: *Msx1* and *Prrx1*. Error bars represent data as mean ± SD from three independent experiments with triplicates. Statistics: two-tailed unpaired Student's *t* test. **P* < 0.05 and *****P* < 0.0001. n.s., not significant.

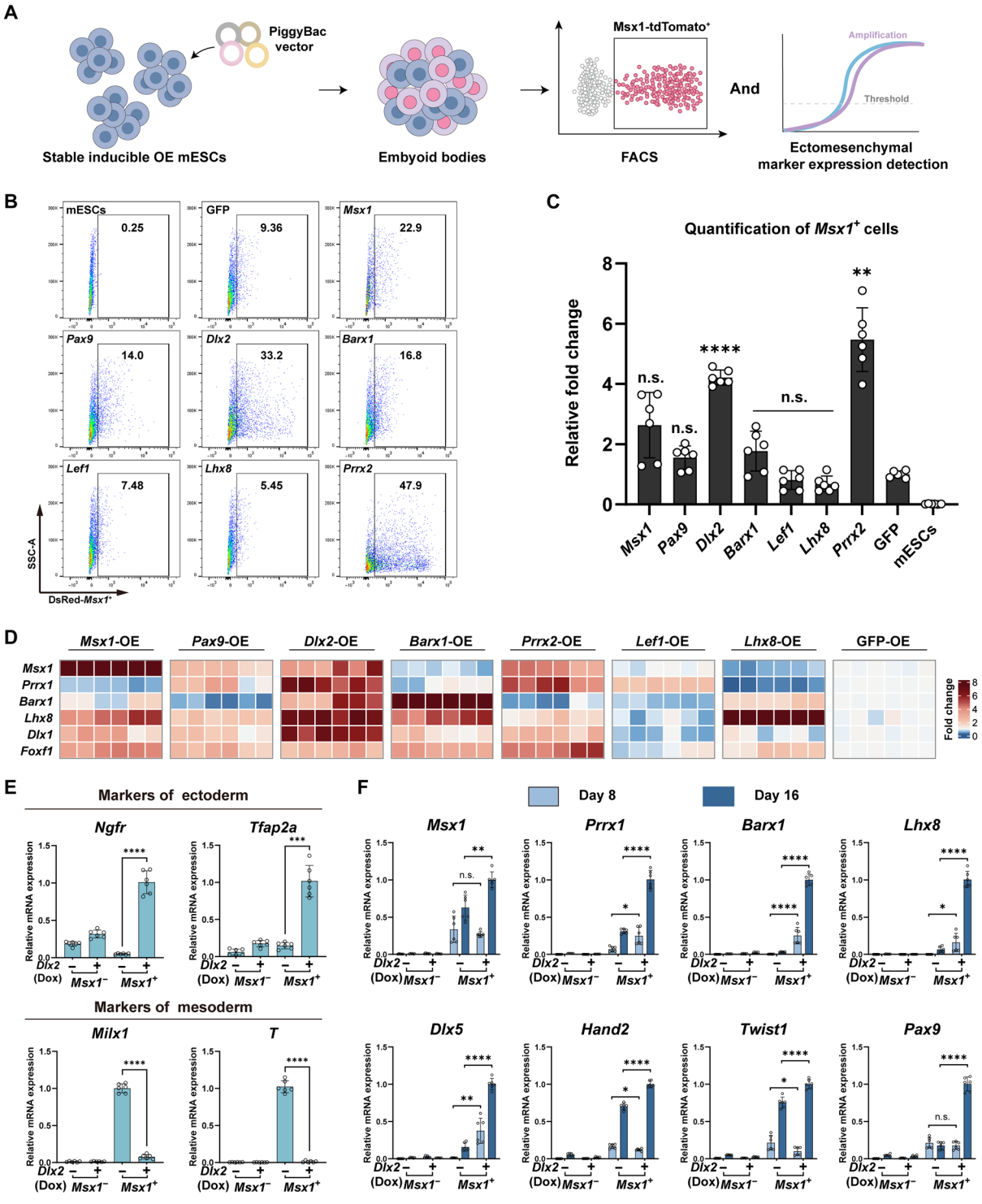

Fig. 2. Screening and characterization of TFs regulating ectomesenchymal differentiation from mESCs. (**A**) Workflow for screening TFs that promoted ectomesenchymal differentiation of mESCs. (**B**) Flow cytometry analysis of *Msx1*$^+$ (tdT$^+$) cells derived from day-8 EBs following OE of TFs. GFP-OE served as the control. SSC-A, side scatter-area. (**C**) Quantification of the fold change (FC) in the proportion of *Msx1*$^+$ cells relative to the GFP-OE group. Error bars represented data as mean ± SD from three independent experiments with duplicates. Statistics: one-way analysis of variance (ANOVA) with Dunnett's post hoc test. (**D**) Heatmap showing the expression of ectomesenchymal marker genes in day-8 EBs following TF-OE, as measured by RT-qPCR. Data represented three independent experiments with biological duplicates. (**E**) Gene expression analysis in sorted cells derived from day-8 EBs. Error bars represented data as mean ± SD from two independent experiments with triplicates. Statistics: two-tailed unpaired Student's *t* test. (**F**) Expression of ectomesenchymal markers in *Msx1*$^+$ and *Msx1*$^-$ cells sorted from day-8 and day-16 EBs. Error bars represented data as mean ± SD from two independent experiments with triplicates. Statistics: two-tailed unpaired Student's *t* test. **P* < 0.05, ***P* < 0.01, ****P* < 0.001, and *****P* < 0.0001. n.s., not significant.

significantly enhances craniofacial gene expression in zebrafish in vivo, leading to craniofacial malformations.

Msx1$^+$ ectomesenchymal progenitors exhibited strong osteochondral differentiation potential as a group

Because ectomesenchyme generates craniofacial skeleton, suture and connective tissues (*2*, *30*–*33*), to further characterize *Dlx2*-induced *Msx1*$^+$ ectomesenchymal progenitors, tdT$^+$ cells were sorted from day-8 and -16 samples, respectively, and subject to bulk RNA transcriptome analysis [RNA sequencing (RNA-seq)] and osteochondral differentiation in vitro and in vivo (Fig. 3A). With Dox induction, *Dlx2*-OE EBs showed strong tdT expression since day 2, and tdT$^+$ cells could be readily observed at days 8 and 16, which was in sharp contrast to samples without Dox induction (fig. S4A). Transcriptome analysis comparing *Msx1*$^+$ (tdT$^+$) versus *Msx1*$^-$ (tdT$^-$) at days 8 and 16 identified significantly differentially expressed genes (DEGs) (fig. S4, B and C), and Gene Ontology (GO) analysis suggested that these genes were mainly involved in pattern specification, mesenchyme differentiation, and skeletal development (fig. S4D). Only *Dlx2*-induced *Msx1*$^+$ cells were enriched with a list of ectomesenchymal markers without detectable expression of limb ones (Fig. 3B and fig. S4E). Immunostaining of VIMENTIN further supported the mesenchymal state for *Msx1*$^+$ cells, but not *Msx1*$^-$ ones (Fig. 3C). Chondrogenic and osteogenic differentiation in vitro indicated that *Msx1*$^+$ cells, as a group, had strong osteochondral differentiation potential (Fig. 3D), which increased over time (fig. S4F). When sorted *Msx1*$^+$ and *Msx1*$^-$ cells were transplanted under kidney capsule, only *Msx1*$^+$ cells generated tissues containing large areas of cartilage and bones (Fig. 3E), which could be further confirmed through SOX9 (transcription factor SOX-9), COL2A1 [collagen alpha-1(II) chain], RUNX2 (runt-related transcription factor 2), and COL10A1 [collagen alpha-1(X) chain] immunostaining (Fig. 3F) and microcomputed tomography (μCT) (Fig. 3G) and Masson's trichrome staining (Fig. 3H). Furthermore, transplantation of *Msx1*$^+$ cells into the mandibular defect area resulted in the formation of new bones (Fig. 3, I and J). Quantitative analysis revealed that mineralized tissue was substantially higher in the *Msx1*$^+$ cell group compared to the *Msx1*$^-$ and control groups (Fig. 3K). Together, these data supported that the *Dlx2*-induced *Msx1*$^+$ progenitors expressed specific ectomesenchymal lineage markers and, as a group, retained strong osteochondral differentiation potential in vitro and in vivo.

Dlx2-induced differentiation recapitulated the cranial neural crest-to-ectomesenchyme developmental trajectory

To investigate whether *Dlx2*-induced ectomesenchymal differentiation would follow the known cranial neural crest-to-ectomesenchymal developmental trajectory, we harvested EBs at four stages (days 2, 8, 12, and 16) for single-cell RNA sequencing (scRNA-seq) (Fig. 4A). Combined scRNA-seq analyses of the above mentioned four stages identified 15 cell compositions with distinct cellular markers (Fig. 4, B and C). Among them, clusters 0 to 6 corresponded to development-relevant cell populations. Specifically, cluster 0 represented the starting mESCs due to high expression of *Pou5f1* and *Nanog*. Cluster 1 was identified as neural tubelike cells with *Hoxa1* and *Gbx2* expression (*34*, *35*). Clusters 2 and 3 corresponded to pre-EMT and delaminating CNCCs as marked by *Pax3*, *Zic1*, *Dlx5*, and *Bmper* (*34*, *36*, *37*). Cluster 4 represented migratory CNCCs and ectomesenchyme, marked by *Snai1/2*, *Twist1*, and *Msx1* (*34*, *36*, *38*, *39*). Last, cluster 5 was identified as skeletogenic progenitors as marked by *Sox9* and *Runx2*, while cluster 6 represented vascular smooth muscle cells (VSMCs), marked by *Myh11* and *Cnn1* (fig. S5A) (*40*, *41*). Pseudotime and RNA velocity both indicated gradual differentiation from clusters 0 to 6 (Fig. 4, D and E, and fig. S5B). Key cellular and biological processes, as well as critical regulators along the differentiation trajectory, indicated that the *Dlx2*-induced ectomesenchymal differentiation indeed followed known developmental programs (Fig. 4, F and G).

DLX2 directly bound LAP2-dependent nuclear chaperoning system

To dissect the molecular mechanism of *Dlx2*-induced ectomesenchymal differentiation, we constructed a Dox-inducible FLAG-tagged *Dlx2* transposon vector (fig. S6A) and confirmed that the FLAG-tagged *Dlx2* could induce similar ectomesenchymal differentiation as wild-type (WT) *Dlx2* gene (fig. S6, B and C). We then used the vector for immunoprecipitation (IP) in EBs and subsequent mass spectrometry analysis (Fig. 5A). FLAG-IP (DLX2) samples were compared with both immunoglobulin G (IgG) and FLAG-IP without Dox controls, and a panel of distinct potential candidates was identified (Fig. 5B). Among these candidates, two protein groups were most interesting to us, one with lamin interacting LAP2 and barrier-to-autointegration factor (BANF1) and the other with nucleosome components histone 2 (H2), H3, and H4 (Fig. 5B). LAP2 was known to directly interact with BANF1 through its LAP2α-Emerin-MAN1 (LEM) domain (*42*), and its isoforms (LAP2α/β) formed a nuclear chaperoning system that guided zinc finger protein GLI1 (GLI1) movement in nucleoplasm and downstream regulatory function (*43*). Coimmunostaining of FLAG and pan-LAP2, LAP2α, and LAP2β antibodies confirmed that DLX2 exhibited colocalization with both LAP2 isoforms (Fig. 5C). FLAG-DLX2 IP also confirmed direct binding with both LAP2α and LAP2β (Fig. 5D). Reciprocally, IP with pan-LAP2 antibody could also pull down FLAG-DLX2 (Fig. 5E). As DLX2 protein could be largely divided into three regions, N-terminal, C-terminal, and a homeodomain connecting the two, we generated several truncation mutants to investigate the potential domain mediating DLX2-LAP2 interactions (Fig. 5F). Neither N- nor C-terminal deletion mutants (ΔN and ΔC) showed any impact on DLX2-LAP2 interactions (Fig. 5G). However, the homeodomain mutant (ΔHD) strongly abolished DLX2's binding with both LAP2α and LAP2β (Fig. 5G). Within the homeodomain, the nuclear localization signal (NLS) was identified as the mediator for LAP2β binding, while the rest of 38–amino-acid polypeptide was critical for LAP2α (Fig. 5G). To further confirm it, we generated a structural model of the DLX2-LAP2α complex using AlphaFold 3 (*44*). The predicted structure suggested that DLX2 fit into a groove on LAP2α, thereby facilitating their interaction. Notably, DLX2 residues Gln204 (Q204), Ser208 (S208), Lys211 (K211), and Lys212 (K212) within the HD domain were predicted to form specific contacts with LAP2α residues Tyr621 (Y621), Asp622 (D622), Ser625 (S625), and Asp629 (D629) (Fig. 5H). We also validated the DLX2-LAP2α interaction in facial prominences of E10.5 embryos (fig. S6D), further supporting the physiological relevance of this binding in craniofacial development. We observed that the nuclear lamina localization of DLX2 was not required for LAP2α binding, as colocalization of DLX2 and lamin-B1 (LMNB1) between WT and NLS mutant did not show significant differences (fig. S6, E and F). Unlike GLI1 where only acetylated GLI1 could

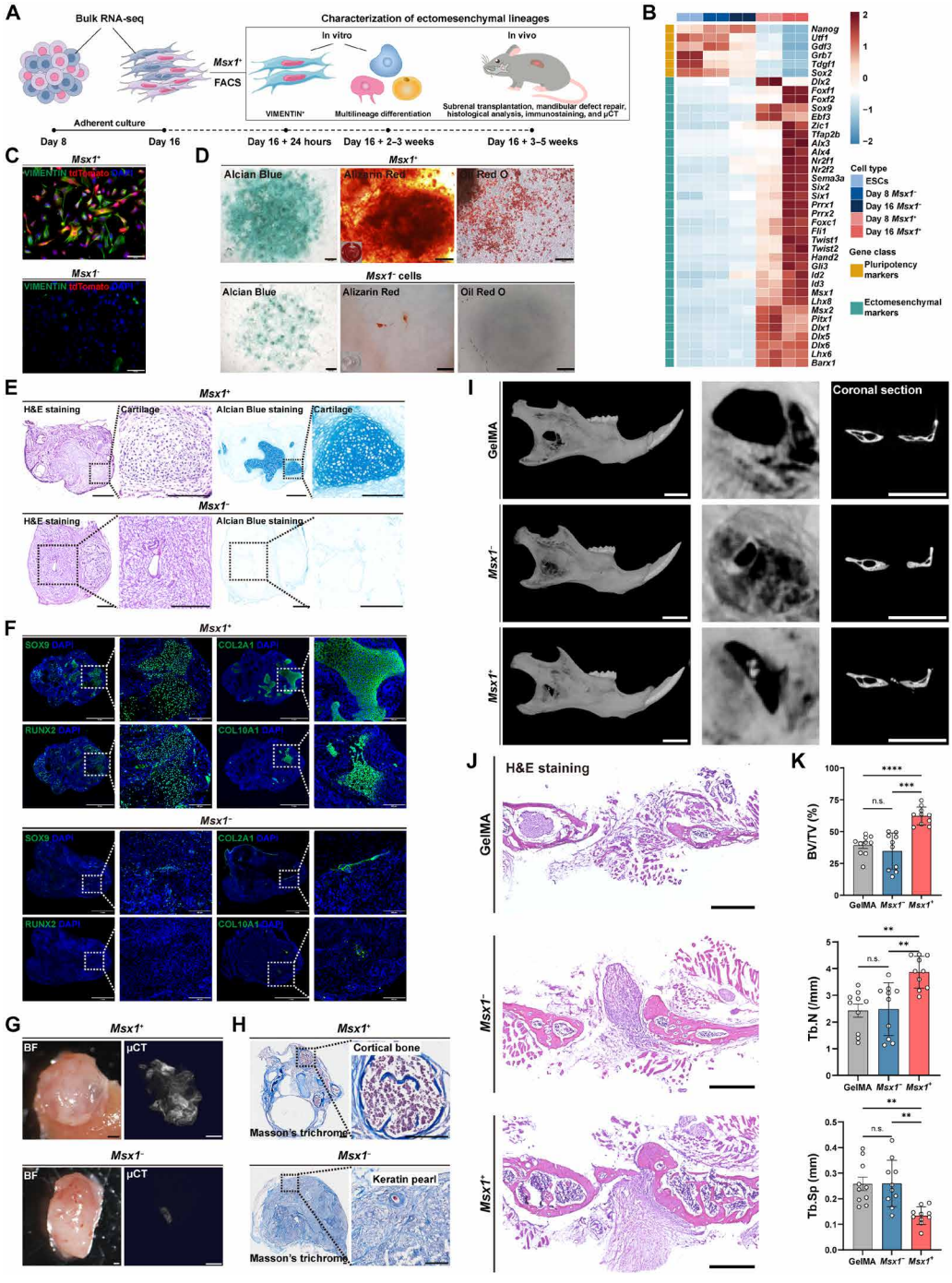

Fig. 3. Characterization of *Msx1*$^+$ cells derived from *Dlx2*-OE EBs. (**A**) The experimental strategy for validating the ectomesenchymal identity of *Dlx2*-OE *Msx1*$^+$ cells. (**B**) Bulk RNA-seq analysis of *Msx1*$^+$ and *Msx1*$^-$ cells sorted from day-8 and -16 EBs. The heatmap displayed transcripts per million–based gene expression levels across groups, with pluripotency markers shown in yellow and ectomesenchymal markers shown in green. (**C**) Immunostaining of VIMENTIN. DAPI was used for nuclear staining. Scale bars, 100 μm. (**D**) In vitro differentiation assays of *Msx1*$^+$ and *Msx1*$^-$ cells. Cells were sorted from day-16 EBs. Alcian Blue staining identified chondrocytes, Alizarin Red staining detected calcium deposits in osteoblasts, and Oil Red O staining visualized adipocytes. Scale bars, 200 μm (Alizarin Red and Oil Red O) and 500 μm (Alcian Blue). (**E**) Hematoxylin and eosin (H&E) and Alcian Blue staining of *Msx1*$^+$ and *Msx1*$^-$ cells 3 weeks after renal capsule transplantation. Scale bars, 500 μm and 200 μm (zoom-in). (**F**) Immunostaining of transplanted cells 3 weeks post–renal capsule transplantation. Chondrocyte markers: SOX9 and COL2A1. Osteoblast markers: RUNX2 and COL10A1. Scale bars, 1 mm and 200 μm (zoom-in). (**G** and **H**) μCT analysis and Masson's trichrome staining of transplanted cells, 5 weeks after renal capsule transplantation. BF, bright field; BM, bone marrow. Scale bars, 500 μm (G) and 200 μm (H). (**I**) Three-dimensional (3D)–reconstructed and coronal single-section μCT images of mandibular bone defects at 5 weeks posttransplantation; $n = 10$ per group. Scale bars, 2 mm. (**J**) H&E staining in coronal sections of mandibles. Scale bars, 500 μm. (**K**) Quantification of bone formation parameters at defect regions; $n = 10$ per group. Statistics: one-way ANOVA with Tukey's post hoc test. $^{**}P < 0.01$, $^{***}P < 0.001$, and $^{****}P < 0.0001$. n.s., not significant.

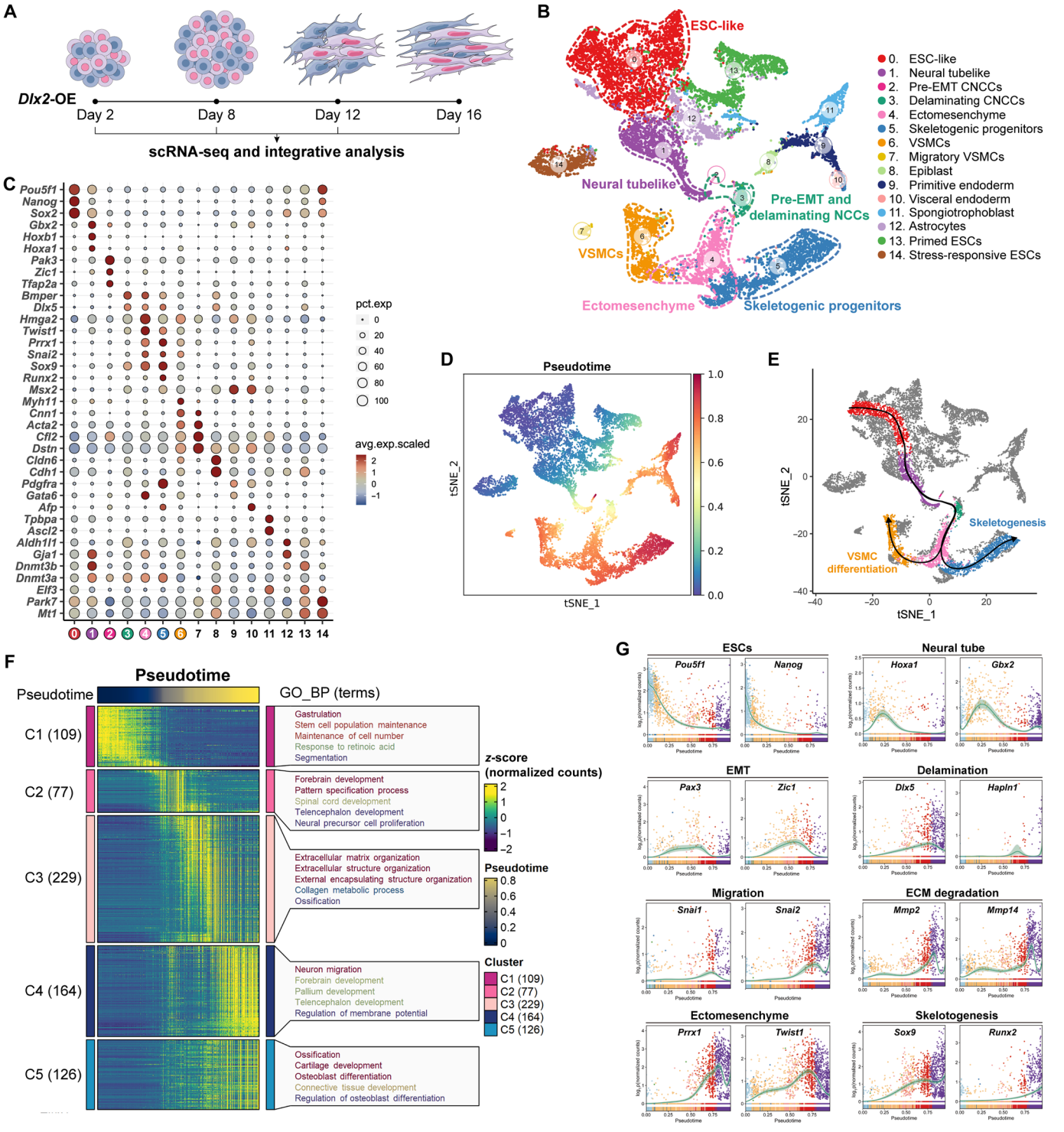

Fig. 4. scRNA-seq analysis of *Dlx2*-induced ectomesenchymal differentiation. (**A**) Schematic of the scRNA-seq experimental design. (**B**) t-distributed stochastic neighbor embedding (t-SNE) visualization of 15 distinct cell clusters based on harmony-integrated data, with key lineage-specific populations highlighted by dashed lines. Cluster annotations are shown on the right. (**C**) Dot plot showing expression profiles of marker genes across 15 clusters. Dot size represented the percent expression (pct. exp) of cells per cluster, and color reflected average scaled expression (avg.exp.scaled) levels. Key clusters of interest were highlighted, with color consistent with (B). (**D**) Pseudotime of ESC-derived lineages projected on t-SNE coordinates, with blue to red colors indicating early to late values. (**E**) Skeletogenesis and VSMC differentiation trajectories [colored as in (B)] with directions indicated by arrows. (**F**) Dynamic genes clustering and GO analysis based on pseudotime ordering of cells in the skeletogenesis trajectory. (**G**) Pseudotemporal gene expression dynamics during skeletogenesis revealed stage-specific expression patterns. ECM, extracellular matrix.

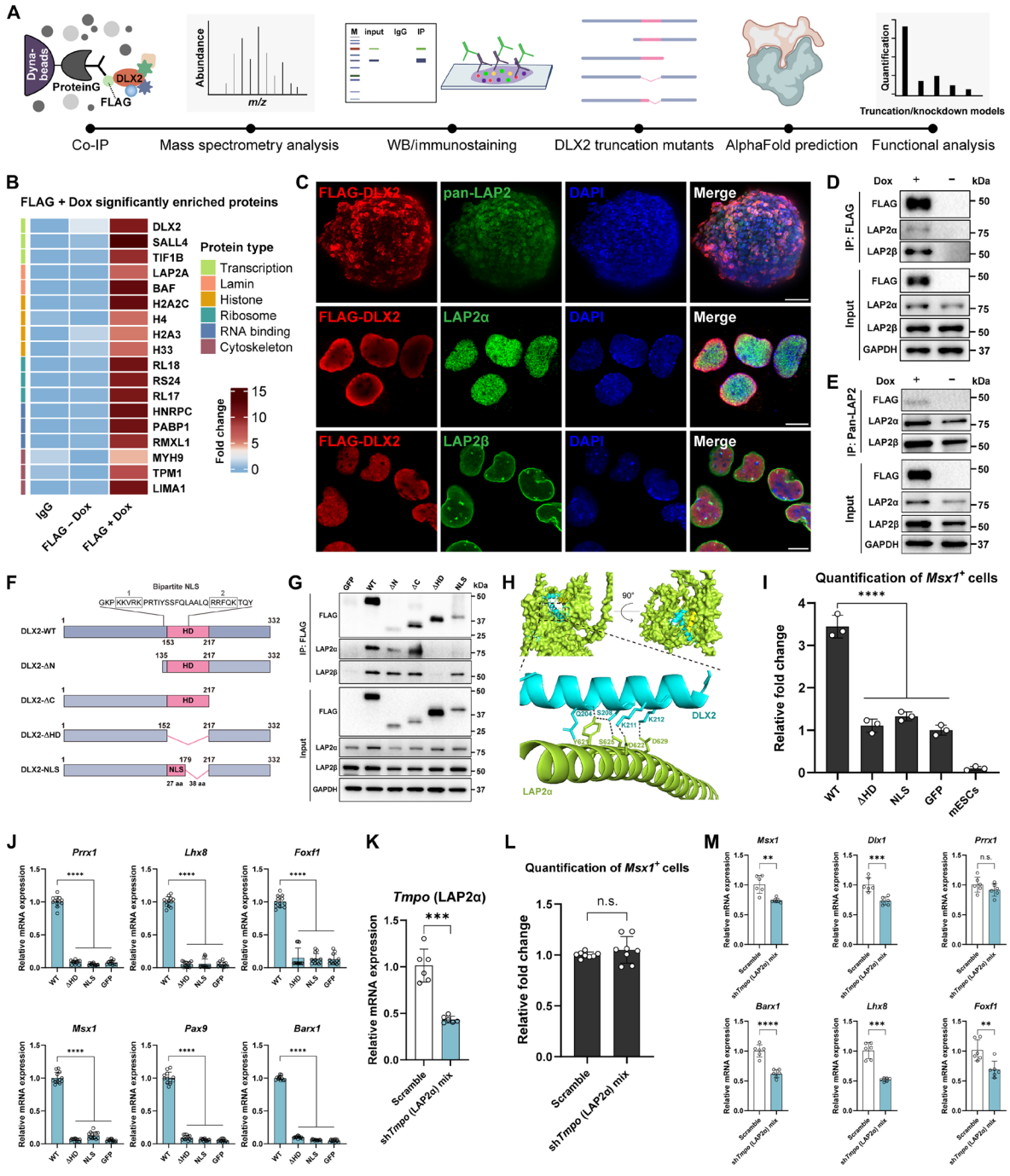

Fig. 5. Analysis of DLX2 and LAP2 interactions in ectomesenchymal differentiation. (**A**) Schematic of FLAG-tagged DLX2-binding partner identification and validation. *m/z*, mass/charge ratio; WB, Western blot. (**B**) Liquid chromatography–mass spectrometry (LC-MS) heatmap of day-2 *Dlx2*-OE (FLAG +Dox) EBs. Proteins were labeled by UniProt entry names, with FC indicated by color intensity (red). (**C**) Immunostaining of *Dlx2*-OE cells. DAPI for nuclear staining. Scale bars, 50 μm (EBs) and 10 μm (single cells). (**D** and **E**) Co-IP of DLX2 and LAP2 isoforms in day-2 *Dlx2*-OE EBs. Glyceraldehyde-3-phosphate dehydrogenase (GAPDH) as the loading control. (**F**) Schematic of DLX2 truncation mutants: WT and four mutants with deletions in the N-terminal (ΔN), C-terminal (ΔC), homeodomain (ΔHD), or 38 amino acids in the homeodomain, retaining the NLS. aa, amino acids. (**G**) Co-IP of LAP2α, LAP2β, and FLAG-DLX2 mutants in day-2 EBs using anti-FLAG antibody. (**H**) Predicted DLX2-LAP2α protein complex structure. (**I**) Flow cytometry quantification of *Msx1*$^+$ cells in day-8 EBs. Data shown as mean ± SD from three independent experiments. Statistics: one-way ANOVA with Dunnett's post hoc test. (**J**) RT-qPCR of ectomesenchymal marker genes in day-8 EBs. Data shown as mean ± SD from three independent experiments. Statistics: one-way ANOVA with Dunnett's post hoc test. (**K**) RT-qPCR of *Tmpo* KD efficiency in day-8 *Dlx2*-OE EBs, with two shRNA mix delivered into cells. Data shown as mean ± SD from three independent experiments. Statistics: two-tailed unpaired Student's *t* test. (**L**) Flow cytometry quantification of *Msx1*$^+$ cells in day-8 *Dlx2*-OE EBs with *Tmpo* KD. Data shown as mean ± SD from four independent experiments. Statistics: one-way ANOVA with Dunnett's post hoc test. (**M**) RT-qPCR of ectomesenchymal marker genes in day-8 *Dlx2*-OE EBs with *Tmpo* KD. Data shown as mean ± SD from three independent experiments. Statistics: two-tailed unpaired Student's *t* test. $^{**}P < 0.01$, $^{***}P < 0.001$, and $^{****}P < 0.0001$. n.s., not significant.

bind LAP2α (*43*), no substantial acetylation was detected from DLX2 (fig. S6G). Moreover, loss of LAP2α interaction largely diminished DLX2-induced *Msx1*$^+$ ectomesenchymal differentiation as revealed by FACS (Fig. 5I), which was further confirmed by strongly decreased expressions of craniofacial markers (Fig. 5J). To distinguish whether this effect specifically resulted from the loss of DLX2-LAP2α binding, rather than from a general functional impairment caused by deleting the 38–amino-acid motif, we knocked down LAP2α expression using shRNAs (Fig. 5K). While LAP2α KD did not significantly affect the percentage of *Msx1*$^+$ cells or the expression of the general mesenchymal maker *Prrx1*, it led to significant down-regulation of other craniofacial markers (Fig. 5, L and M). Together, these data indicated that DLX2 functioned through direct binding with LAP2-dependent nuclear chaperoning system, and its interaction with LAP2α was particularly important for ectomesenchymal differentiation.

Interaction between DLX2, LAP2α, and nucleosomes promoted open chromatin

As IP–mass spectrometry analysis also identified nucleosome components as potential interaction candidates, IP with FLAG-DLX2 antibody was used to validate the DLX2-LAP2α-nucleosome interaction. Full-length DLX2 (WT) showed strong interaction with representative nucleosome components, including H2A and H4, and this interaction was lost when the 38–amino-acid LAP2α-binding polypeptide was deleted (Fig. 6A). Co-IP in the presence of ethidium bromide (EtBr), which inhibits indirect interactions via DNA binding, and Benzonase nuclease, which degrades chromosomal DNA and RNA (*45*–*47*), further confirmed this interaction (fig. S7A). Meanwhile, according to the 4′,6-diamidino-2-phenylindole (DAPI) signal, the chromatin could be divided into two regions: the DAPI-dispersed region (euchromatin) or DAPI-dense region (heterochromatin) (*48*). FLAG-DLX2 immunostaining indicated that DLX2 did not colocalize with the DAPI-dense heterochromatin (Fig. 6, B and C). Further staining and quantitative analysis revealed that when compared with GFP control, full-length *Dlx2* OE significantly reduced the number of nuclear DAPI-dense foci. This effect was diminished not only by loss of LAP2α binding (NLS mutant) but also upon LAP2α KD, supporting that the DLX2-LAP2α interaction contributed to chromatin decompaction (Fig. 6, D and E, and fig. S7, B to D). To examine how the binding of DLX2 affected the chromatin state, we performed the CUT&Tag analysis of DLX2, H3K27ac (histone H3 lysine 27 acetylation, open chromatin marker), and H3K9me3 (histone H3 lysine 9 trimethylation, heterochromatin marker) (*49*) in the *Dlx2*-OE and control cells. Genome-wide analysis showed a pronounced increase in H3K27ac signals but a decrease in H3K9me3 signal on the DLX2-binding sites in the *Dlx2*-OE cells, compared with the control (Fig. 6F). Together, these data supported that the interaction between DLX2, LAP2α, and nucleosomes promoted open chromatin.

DLX2-LAP2α coregulated an ectomesenchymal gene network

Next, we sought to identify the downstream regulatory mechanisms for *Dlx2*-induced ectomesenchymal differentiation using an integrative multiomic approach (Fig. 7A). First, DEGs between *Dlx2*-OE and GFP-OE control were identified by bulk RNA-seq (Fig. 7B). GO analysis revealed that these genes were mainly involved in pattern specification, mesenchyme development, and cell fate commitment (Fig. 7C). In addition, CUT&Tag analysis using FLAG and LAP2α antibodies revealed genome-wide binding sites of DLX2 and LAP2α (Fig. 7, D and E, and fig. S8, A and B) and respective enriched motifs (Fig. 7F and fig. S8C). Integrative analysis then identified 255 overlapping genes from these three datasets (Fig. 7G), most of which were activated upon *Dlx2*-OE (fig. S8D). Statistical analyses confirmed that the number of genes cobound and coregulated (DEGs) by DLX2 and LAP2α substantially exceeded random overlap (fig. S8E). GO analysis of the 255 coregulated genes revealed significant enrichment of ectomesenchyme-related terms, including skeletal system morphogenesis, pattern specification, and mesenchymal development (fig. S8F). Among these identified genes, there were several known modulators of craniofacial development, such as *Dlx6* (*2*, *50*–*54*), *Msx2* (*22*, *51*, *55*–*57*), *Gata4* (*58*, *59*), and *Hmga2* (*2*, *60*–*62*). These genes were cobound by DLX2 and LAP2α (Fig. 7H and fig. S8G). RT-qPCR analysis and increased H2K27ac signals further validated their activated transcription state (fig. S8, H and I). To investigate whether these genes were involved in *Dlx2*-induced *Msx1*$^+$ ectomesenchymal differentiation, we knocked down the genes by shRNAs in ESCs, and KD cells were subjected to EB differentiation (Fig. 7I). Flow cytometry analysis confirmed that *Msx1*$^+$ ectomesenchymal differentiation was compromised in KD cells (Fig. 7, J and K). RT-qPCR analysis further confirmed the down-regulation of craniofacial marker expression in KD cells (Fig. 7L). Notably, *Kif15* and *Trpc5os*, which were only bound by DLX2, were not affected by *Tmpo* (LAP2α) KD (fig. S8J). Together, these data indicated that DLX2 and LAP2α coregulated an ectomesenchymal oriented regulatory network, interference of which would substantially compromise ectomesenchymal differentiation.

The high conservation of *Dlx* family genes across vertebrates led us to hypothesize that other *Dlx* family members may also promote ectomesenchymal differentiation. To investigate this, we overexpressed all six *Dlx* genes individually in mESCs and the derived EBs (fig. S9A). Flow cytometry and marker gene expression analyses revealed that among the family members, *Dlx2*, *Dlx3*, and *Dlx5* exhibited the most significant effects on both *Msx1*$^+$ cell generation and ectomesenchymal marker expression, although *Dlx3* and *Dlx5* were less potent than *Dlx2* (fig. S9, B to D). These findings suggested that DLX2, DLX3, and DLX5 might share conserved roles in regulating an ectomesenchymal differentiation network. Furthermore, KD of *Dlx2* in *Dlx3*-OE EBs resulted in reduced ectomesenchymal marker expression, as assessed by flow cytometry and RT-qPCR, underscoring *Dlx2*'s critical role in this process (fig. S9, E to H).

DISCUSSION

In this study, we identified *Dlx2* as a potent regulator that could induce *Msx1*$^+$ ectomesenchymal differentiation from ESCs. The *Dlx2*-induced ectomesenchymal specification followed the known developmental trajectory, and the *Msx1*$^+$ ectomesenchymal progenitors not only expressed key craniofacial markers but also exhibited strong osteochondral differentiation potential, a key feature for the developing ectomesenchyme in vivo. Mechanistically, we found that DLX2 directly interacted with the LAP2-dependent chaperoning system. By forming a DLX2-LAP2α-nucleosome complex through a 38–amino-acid polypeptide, DLX2 promoted the chromatin opening, activated the transcription of ectomesenchymal lineage regulatory network, and drove the differentiation (Fig. 8).

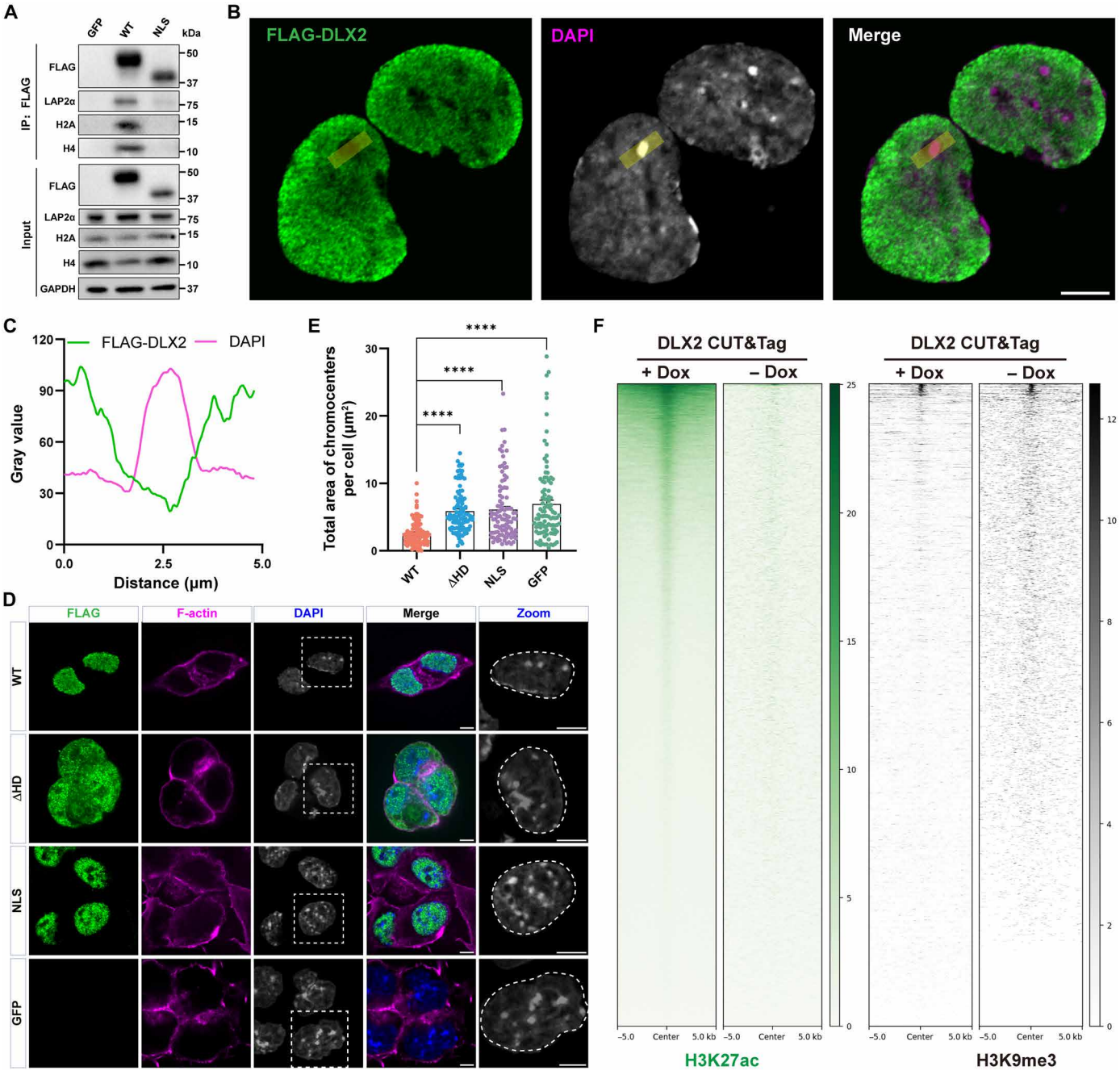

Fig. 6. DLX2 unpacked condensed heterochromatin in ectomesenchymal differentiation. (**A**) Co-IP assay showing the association between DLX2 and nucleosomes. GAPDH served as the loading control. (**B**) Subnuclear localization of FLAG-tagged DLX2 in *Dlx2*-OE cells. DAPI was used for nuclear staining. Scale bar, 5 μm. (**C**) Quantification of fluorescence intensity of FLAG-DLX2 and DAPI signal along the line indicated in (B). (**D**) Representative images of mESCs overexpressing FLAG-DLX2 (WT) and two truncation mutants (ΔHD and NLS), with GFP-OE cells as the control. DAPI was used for nuclear staining. Dashed lines indicated the nuclear perimeter. Scale bars, 5 μm. (**E**) Quantitative analysis of the DAPI-dense regions in (D). Each dot represented a single cell; $n = 100$ per group. Error bars represented data as mean ± SD from three independent experiments with triplicates. Statistics: one-way ANOVA with Dunnett's post hoc test. ****$P < 0.0001$. (**F**) Heatmaps showing the marked changes of DLX2-binding signals at H3K27ac (left) and H3K9me3 (right) sites in the day-2 *Dlx2*-OE EB cells and the control cells. The signal was sorted by the H3K27ac (left) and H3K9me3 (right) peaks.

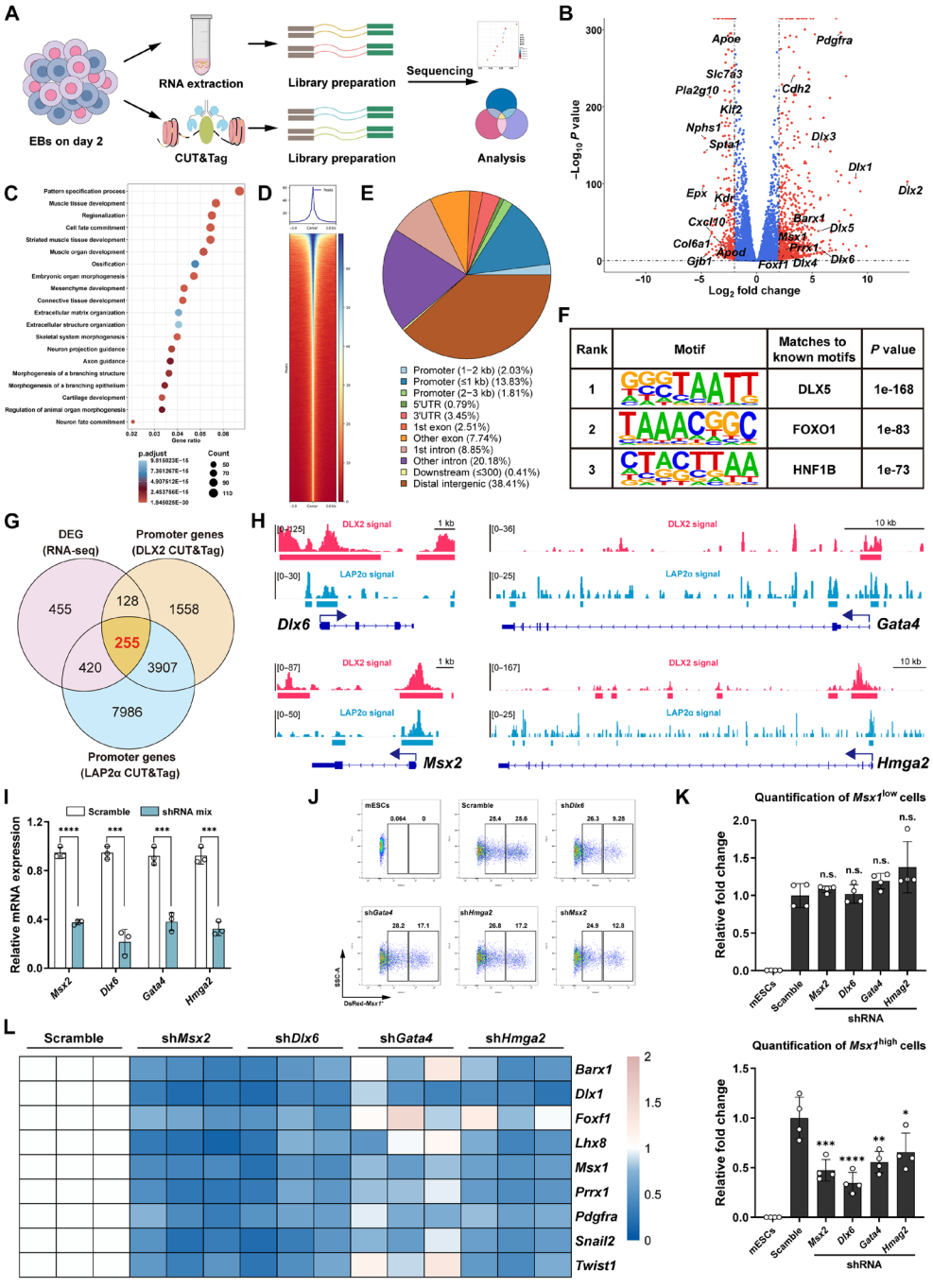

Fig. 7. Integrative analysis identified the downstream regulatory network of *Dlx2* in ectomesenchymal differentiation. (**A**) Schematic of integrative analysis combining RNA-seq and CUT&Tag data. (**B**) DEG analysis between *Dlx2*- and GFP-OE control cells. DEGs were identified with DESeq2 ($log_2FC \geq 2$ and $P < 0.05$) and included multiple ectomesenchymal markers. (**C**) GO analysis of up-regulated genes in *Dlx2*-OE cells. The top 20 GO terms displayed in the dot plot. (**D**) Heatmap of a genome-wide overview of DLX2-binding sites identified by CUT&Tag. Each row represented a 3-kb window centered on the peak midpoint. (**E**) Pie chart showing the genomic distribution of DLX2-binding sites. 3′UTR, 3′ untranslated region. (**F**) HOMER analysis of known DNA sequence motifs enriched at significant DLX2-binding peaks. (**G**) Venn diagram showing overlap of promoter-proximal DLX2- and LAP2α-binding targets with DEGs from RNA-seq. (**H**) Representative Integrative Genomics Viewer tracks of DLX2 and LAP2α signals at promoter regions of target genes. (**I**) KD efficiency of target genes assessed by RT-qPCR in day-8 *Dlx2*-OE EBs, with three shRNA mix delivered via the PB transposon system. Error bars represented data as mean ± SD from three independent experiments. Statistics: two-tailed unpaired Student's *t* test. (**J** and **K**) Flow cytometry analysis of $Msx1^+$ cell proportions in day-8 EBs after KD of target genes, showing representative plots (J) and quantitative FC in $Msx1^{low}$ and $Msx1^{high}$ populations relative to scramble control (K). Error bars represented data as mean ± SD from three independent experiments. Statistics: one-way ANOVA with Dunnett's post hoc test. (**L**) RT-qPCR of ectomesenchymal marker gene expression in day-8 *Dlx2*-OE EBs with *Dlx6*, *Hmga2*, *Msx2*, or *Gata4* KD. Heatmap showed relative expression levels compared to scramble control: blue (<1), and pink (>1). Data represented mean ± SD from three independent experiments. *$P < 0.05$, **$P < 0.01$, ***$P < 0.001$, and ****$P < 0.0001$. n.s., not significant.

These data indicated that DLX2 might function as a pioneer factor for ectomesenchymal specification from mESCs.

Development of the "new head" by neural crest may represent a major event during evolution of the vertebrate (*1*). Defects in these craniofacial mesenchymal components can lead to severe developmental disorders, including craniosynostosis, hemifacial microsomia, and Treacher-Collins syndrome (*63*), profoundly affecting patients' quality of life. Regenerative strategies using ectomesenchymal progenitors offer promising therapeutic venues, as demonstrated by recent studies showing that transplanted craniofacial stem cells can ameliorate craniosynostosis (*7*). While substantial progress has been made in deriving neural crest stem cells from pluripotent stem cells, the molecular mechanisms governing their further specification into ectomesenchyme remain poorly understood. The identification of *Dlx2* as a key regulator of ectomesenchymal fate commitment provides critical insights into this process, which may pave the way for more efficient generation of ectomesenchymal progenitors, advancing their potential applications in craniofacial regeneration.

The LAP2-dependent chaperoning system has emerged as a critical regulator of nuclear DLX2 trafficking and downstream transcriptional control, revealing its previously underappreciated role in lineage specification. Previously, GLI1, a key TF in Sonic Hedgehog signaling, was the only known TF reported using LAP2α/β for nuclear shuttling and stem cell fate determination (*43*, *64*). Unlike GLI1, which requires acetylation for LAP2α binding, DLX2 uses a distinct mechanism by directly interacting with LAP2α via a 38–amino-acid polypeptide motif within its homeodomain. Disrupting such interaction severely compromises ectomesenchymal differentiation, highlighting its functional necessity. Notably, this 38–amino-acid sequence is highly conserved among multiple craniofacial TFs, including DLX1/3/4/6, homeobox protein MSX-2 (MSX2), and homeobox protein MSX-1 (MSX1, also known as HOX7), suggesting that the LAP2-dependent chaperoning system may represent a shared regulatory mechanism coordinating multiple TFs to drive mesenchymal specification and craniofacial patterning during embryogenesis. Given that both DLX2 and GLI1 use LAP2α as a nuclear chaperone, it is plausible that loss of DLX2-LAP2α interaction could indirectly affect chromatin organization by altering LAP2α availability for GLI1 or other transcriptional regulators, which warrants further investigations.

Our findings also reveal an intriguing feedback regulatory potential between DLX2 and MSX1. During molar mesenchyme development, MSX1 has been shown to maintain DLX2 expression

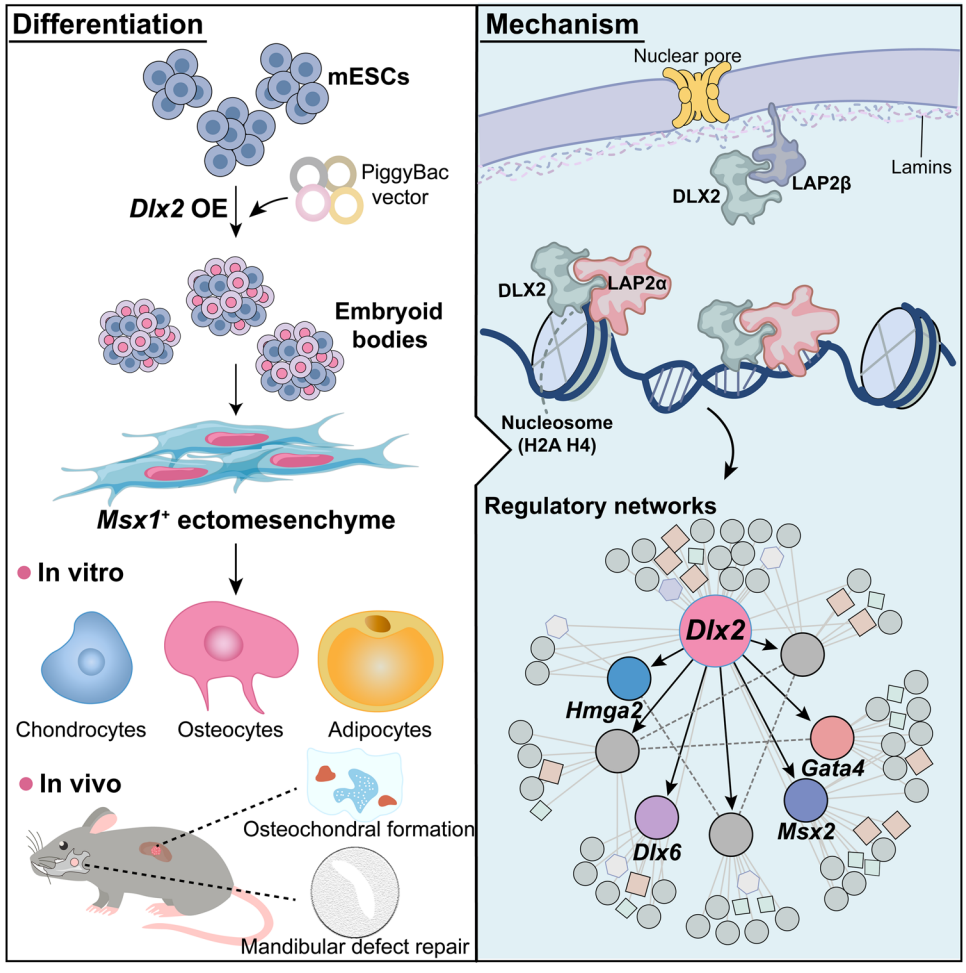

Fig. 8. Graphical summary of the proposed model. Through the formation of a DLX2-LAP2α-nucleosome complex that remodeled chromatin, DLX2 drove ectomesenchymal specification in mESCs, generating *Msx1*$^{+}$ progenitors with craniofacial regeneration potential.

(*65*), forming a reciprocal regulatory loop important for craniofacial patterning (*66*, *67*). In this context, BMP4 signaling acts upstream of both *Msx1* and *Dlx2*, suggesting that the DLX2-LAP2α axis operates within a broader BMP4-MSX1-DLX network that stabilizes the ectomesenchymal gene program. These insights highlight a conserved transcriptional-epigenetic circuitry in craniofacial mesenchyme involving BMP, *Msx*, and *Dlx* family members.

The functional importance of *Dlx2* dosage in craniofacial morphogenesis has been well documented in vivo. Neural crest–specific *Dlx2* OE in mice induced cleft palate, damaging maxillary development, CNCC proliferation, and osteogenesis (*68*, *69*). *Dlx2* gain of function also enhanced ectomesenchymal adhesion and condensation, contributing to skeletal dysmorphology (*70*). In contrast, *Dlx1/2* KO caused posterior palate outgrowth failure (*71*), alongside proximodistal patterning defects in branchial arches (*72*). While these models underscored *Dlx2*'s dosage sensitivity in vivo, our study revealed its pioneer activity via LAP2α-mediated chromatin remodeling, enabling controlled ectomesenchymal specification in ESCs.

Last, there are several limitations of our study that need further investigations. First, it is still unclear whether the DLX2-LAP2α association is mediated by mutual binding to chromatin or represents a direct protein-protein interaction. Although EtBr, which disrupts nucleosome-DNA interactions, and Benzonase, which degrades genomic DNA, were used individually and in combination in co-IP assays, none of these treatments disrupted the association among DLX2, LAP2α, and histones, indicating that their interaction is not solely dependent on DNA-mediated bridging but likely reflects a stable protein-protein complex. Second, whether the DLX2-LAP2α-nucleosome–mediated mechanism is conserved in human ectomesenchymal differentiation and whether other craniofacial TFs use similar LAP2α-dependent regulation require further investigation. Moreover, the *Dlx2*-induced differentiation still relies on EB formation, which is difficult for generating ectomesenchymal progenitors in scale and controlling the homogeneity. Last, although the *Dlx2*-induced *Msx1*$^{+}$ ectomesenchymal cells are distinct from limb mesenchyme, the specific craniofacial subregion they most closely resemble, such as maxillary, frontonasal, or mandibular mesenchyme, remains to be defined. Clarifying this spatial identity will be essential for refining developmental equivalence and optimizing their regenerative potential.

MATERIALS AND METHODS

Experimental design

Ethical approval

All animal procedures were conducted in accordance with protocols approved by the Institutional Animal Care and Use Committee (IACUC) of the College of Life Sciences, Sichuan University (approval no: 20200401001).

Mouse strains and animal care

Mice were housed under standardized conditions in individually ventilated cages with companion animals, maintained on a 12-hour light/dark cycle at a controlled temperature, and provided ad libitum access to food and water. Mating was performed using mice older than 8 weeks, and the presence of a vaginal plug was designated as E0.5. Embryos were harvested at developmental stages as described in the Results. Knock-in transgenic mice (Msx1$^{P2A\text{-}tdTomato}$) were generated by Biocytogen Inc. (Beijing).

Facial prominences and limb dissection

The facial prominences and limbs were physically separated from the E10.5, E12.5, and E14.5 embryos of Msx1$^{P2A\text{-}tdTomato}$ mice using dissection needles under a stereo-fluorescent microscope (Olympus, SZX10, Japan). The general morphological boundaries of the tissues were first identified according to standard anatomical landmarks described in classic mouse embryology atlases (*73*). Subsequently, tdT fluorescence was used as a guide to refine the dissection, ensuring the precise isolation of Msx1-expressing mesenchymal regions. All dissections were carried out in ice-cold phosphate-buffered saline (PBS; Gibco, catalog no. C10010500BT) to maintain tissue integrity. Isolated tissues were either immediately processed for downstream applications or snap frozen and stored at −80°C.

Cell culture

Msx1-tdTomato mESCs were derived from *Msx1*$^{P2A\text{-}tdTomato}$ mice according to a previously published protocol (*74*). mESCs were maintained on plates pretreated with 0.1% (w/v) gelatin (Sigma-Aldrich, catalog no. G1890-100G) in standard ES medium [Dulbecco's modified Eagle's medium (DMEM; Gibco, catalog no. C11995500BT), 15% (v/v) fetal bovine serum (FBS) (Hyclone, catalog no. SH30084.03), 1% (v/v) MEM nonessential amino acids solution (Gibco, catalog no. 11140050), 1% (v/v) GlutaMAX (Gibco, catalog no. 35050061), 1% (v/v) Penicillin-Streptomycin (Pen-Strep; Gibco, catalog no.15140-122), 0.1 mM 2-Mercaptoethanol (Sigma-Aldrich, catalog no. M3148), and leukemia inhibitory factor (LIF) (1000 U/ml; MedChemExpress, catalog no. HY-P7049)]. Cells were passaged every 2 days using 0.25% trypsin-EDTA (Thermo Fisher Scientific, catalog no. 25200072) and reseeded at a ratio of 1:8. All the cells were maintained under standard culture conditions (37°C, 5% CO_2, and humidified atmosphere).

Construction of stable inducible OE mESC lines

To construct the pPB-TRE3GV-rtTA vector, the TRE3GV promoter and rtTA sequence were cloned into the PB backbone. For inducible OE system construction, full-length cDNAs of target genes (*Msx1*, *Pax9*, *Barx1*, *Lef1*, *Lhx8*, *Prrx2*, *Dlx1*, *Dlx2*, *Dlx3*, *Dlx4*, *Dlx5*, and *Dlx6*), excluding copepod green fluorescent protein (copGFP; GFP), were amplified from mouse tissue–derived cDNA and subcloned into the pPB-TetO-rtTA vector. GFP was subcloned into the vector as an independently gene control. A 3xFLAG tag was inserted into the N terminus of the *Dlx2* coding sequence. Truncation mutants of *Dlx2* (ΔN, ΔC, ΔHD, and NLS) were constructed using the Mut Express II Fast Mutagenesis Kit V2 (Vazyme, catalog no. C214-01) following the manufacturer's instructions. The sequencing of all the cloning plasmids was confirmed by Sanger sequencing [Sangon Biotech (Shanghai) Co. Ltd].

To establish stable inducible OE mESC lines, *Msx1*-tdTomato mESCs at ~80% confluency were dissociated and resuspended in ES medium. Cells were seeded into 0.1% gelatin-coated six-well plates (BIOFIL, catalog no. TCP011006) and cotransfected with the pPB-TetO-rtTA–based construct and the pTTGY-hyPBase–expression plasmid using Lipofectamine 3000 (Invitrogen, catalog no. L3000008). Each well contained 1×10^6 cells. Twenty-four hours posttransfection, the medium was replaced with fresh ES medium, and stable clones were selected using puromycin (1 μg/ml; InvivoGen, catalog no. ant-pr-1) for at least three passages.

RNA interference

For RNA interference (RNAi), the U6 promoter cassette was inserted into the pPB-TRE3GV-*Dlx2*-rtTA vector. shRNA sequences targeting each gene (three per gene) were derived from the RNAi

Consortium library (*75*). Complementary sense and antisense oligonucleotides were annealed and ligated into the pPB-U6-TRE3GV-*Dlx2*-rtTA vector. All constructs were validated by Sanger sequencing. For transfection, equimolar amounts of two or three shRNA plasmids (total of 330 ng) were mixed and cotransfected with 550 ng of pTTGY-hyPBase into *Msx1*-tdTomato mESCs seeded at 1×10^6 cells per well in six-well plates using Lipofectamine 3000. Twenty-four hours posttransfection, cells were cultured in ES medium containing puromycin (1 μg/ml) for selection. All oligonucleotide sequences used for cloning were listed in table S1.

EB formation

For EB formation, stable inducible mESCs were dissociated with 0.25% trypsin-EDTA and resuspended in No LIF medium (LIF-free ES medium) supplemented with Dox (1 μg/ml; Takara, catalog no. 631311) at a final cell density of 1.5×10^5 cells/ml. Droplets (20 μl) of the suspension were dispensed onto the inverted lids of 9-cm culture dishes (BIOFIL, catalog no. MCD110090), generating 80 to 90 EBs per lid. The lids were then placed back onto dishes containing 7 ml of PBS to maintain humidity and incubated at 37°C with 5% CO_2. After 2 days, EBs were harvested and transferred to 10-cm culture dishes (BIOFIL, catalog no. TCD010100) precoated with 2% (w/v) PolyHEMA (2-hydroxyethyl methacrylate) (Sigma-Aldrich, catalog no. P3932) at a density of 800 to 900 EBs per dish in 8 ml of Dox-containing No LIF medium. The medium was refreshed every other day. On day 8, EBs were transferred to dishes coated with fibronectin (16.7 μg/ml; Millipore, catalog no. FC010) and cultured under adherent conditions until day 16 for subsequent analyses.

Zebrafish and embryos

Embryos were raised at 28.5°C. Fish maintenance and breeding followed the IACUC protocol, with approval by the Animal Care and Use Committee of West China Hospital, Sichuan University (no. 20220422003).

Construction of dlx2a overexpressing transgenic fish and heat shock

The *dlx2a* coding sequence was cloned from cDNA of WT zebrafish embryos at 6 hours postfertilization using the forward 5′-ATGAAAAACATGACTGGAG-3′ and reverse 5′-TCAAAATATGGTCCCGCGCTAAC-3′ primers. The Tol2 transposon system was used to generate transgenic line. WT zebrafish were self-crossed to obtain embryos, and then the *dlx2a* plasmid and Tol2 transposase mRNA were microinjected into single-cell–stage embryos to ensure stable genomic integration. Transgenic embryos were screened for positive integration using the enhanced GFP (EGFP) reporter. Heat-shock induction was performed by transferring embryos to a 37°C incubator for 30 min at 0.5 days postfertilization (dpf) and 1 hour at 1 dpf, followed by recovery in a standard 28.5°C incubator. To minimize phenotypic variability, the F2 progeny from crosses between F1 Tol2-integrated transgenic fish (with stable transgene integration) and WT zebrafish was used for all heat-shock experiments. The control group consisted of nonfluorescent WT sibling embryos derived from the same heat-shocked clutch. These siblings lacked the *dlx2a*-EGFP transgene and thus did not overexpress *dlx2a* and EGFP, thereby controlling for genetic background and any potential effects of heat shock or culture conditions. Embryos were then fixed at 3.5 dpf in 4% (w/v) paraformaldehyde (PFA; Sigma-Aldrich, catalog no. 158127) overnight at 4°C for subsequent staining.

Histological analysis of zebrafish

At 3.5 dpf, zebrafish were observed for cartilage development by Alcian Blue staining. For each group, a minimum of 10 zebrafish were fixed overnight at 4°C in 4% PFA. After fixation, samples were thoroughly dehydrated in 50% ethanol for 10 min, followed by overnight staining at 4°C with 0.02% staining agent/90% ethanol. The next day, pigments were removed by bleaching with 3% H_2O_2/0.5% KOH solution. Last, the embryos were washed twice with 25% glycerol/0.1% KOH and stored in 100% glycerol at 4°C for imaging.

Fish sample collection for RT-qPCR

For RT-qPCR analysis, *dlx2a*-OE and WT siblings were identified by EGFP fluorescence at 2 dpf, and the cranial region of each fish was dissected under a stereomicroscope. Tissue samples from all OE or WT individuals, regardless of phenotypic severity, were pooled by group for RNA extraction and RT-qPCR.

Flow cytometry

Facial prominences and limbs from the E10.5, E12.5, and E14.5 embryos and EBs were dissociated with 0.25% trypsin-EDTA for 5 to 10 min. To minimize cell clumping, 20 to 50 μl of deoxyribonuclease I (5 mg/ml; Roche, catalog no. 10104159001) was added during dissociation. Tissues and EBs were dissociated into single-cell suspensions by gentle, repeated pipetting and immediately neutralized with an equal volume of No LIF medium. Cells were then centrifuged at 450*g* for 3 min, washed once with 2% (w/v) bovine serum albumin (BSA) (Sigma-Aldrich, catalog no. A3311-10G), and resuspended in PBS. The resulting single-cell suspension was filtered with a 70-μm strainer (Corning, catalog no. 352350) before downstream experiments. WT embryos or mESCs were used as negative controls. Flow cytometry analysis and FACS were performed on a BD FACSAria III system (BD Biosciences, USA). The voltage settings for the tdT detector (DsRed channel) were 600 V for embryonic tissues and 500 V for EBs, respectively, and were calibrated daily using standard cytometer setup and tracking beads to ensure consistency. The data were analyzed by FlowJo (v 10.4).

Cell differentiation assays

Sorted day-8 and -16 *Dlx2*-OE cells were collected by centrifugation at 300*g* for 5 min and resuspended in No LIF medium. For osteogenic differentiation, 1.5×10^5 cells were seeded into 24-well plates (BIOFIL, catalog no. TCP011024) and cultured in 500 μl of No LIF medium overnight. Adherent cells were then cultured in α–minimum essential medium (MEM; Gibco, catalog no. C12571500BT) supplemented with 10% (v/v) FBS, 10 mM β-glycerophosphate (Millipore, catalog no. 35675), 0.1 μM dexamethasone (DEX) (MedChemExpress, catalog no. HY-14648), ascorbic acid (50 μg/ml; Sigma-Aldrich, catalog no. A8960), and 1% (v/v) Pen-Strep for 21 days. The medium was refreshed every 3 days. Day-21 osteogenic cells were fixed with 4% PFA at room temperature (RT) for 10 min and washed twice with PBS. Fixed cells were stained with 2% (w/v) Alizarin Red S (Sigma-Aldrich, A5533) at RT for 5 min to visualize osteogenic mineralization, followed by three washes with PBS to remove excess dye.

For chondrogenic differentiation, the cell suspension was adjusted to a high cell density of 1.67×10^6 cells/ml. A 340-μl droplet was placed at the center of each well in a 24-well plate and incubated at 37°C for at least 40 min to allow cell attachment. Subsequently, 500 μl OF No LIF medium was added to each well. On the following day, the medium was replaced with chondrogenic induction medium consisting of DMEM supplemented with 2% (v/v) FBS, 0.1 μM DEX, 50 μM ascorbic acid, L-proline (50 μg/ml; Sigma-Aldrich, catalog no. P0380), transforming growth factor–β3 (20 ng/ml; Peprotech, catalog no. 100-36E), basic FGF (20 ng/ml; Peprotech, catalog no. 100-18B), 1% (v/v) Insulin-Transferrin-Selenium (ITS-G;

Gibco, catalog no. 41400045), 1% (v/v) sodium pyruvate (Gibco, catalog no. 11360070), and 1% (v/v) Pen-Strep. Cells were cultured for 14 days with medium changes every other day. To evaluate cartilage formation, a 5% (w/v) stock solution of Alcian Blue 8GX (Sigma-Aldrich, catalog no. A5268-100G) was prepared in PBS and subsequently diluted to 1% (w/v) using 0.1 N of HCl. Following fixation, cells were pretreated with 0.1 N of HCl for 2 min, stained with the working solution for 30 min at RT. After staining, cells were rinsed in 0.1 N of HCl for another 2 min and subsequently washed with PBS.

For adipogenic differentiation, 1.0×10^5 cells were seeded into 24-well plates and cultured in 500 μl of No LIF medium overnight. Adherent cells were then maintained in α-MEM supplemented with 10% (v/v) FBS, 1 μM DEX, insulin (1 μg/ml; Solarbio, catalog no. I8830), 0.5 mM 3-isobutyl-1-methylxanthine (Sigma-Aldrich, catalog no. I5879), and 1% (v/v) Pen-Strep for 14 days. The culture medium was replaced every 2 days. Oil Red O staining was performed to assess adipocyte formation according to the manufacturer's instructions (Solarbio, catalog no. G1260).

Renal capsule transplantation

A total of 1.0×10^5 sorted day-16 *Msx1*$^+$ or *Msx1*$^-$ cells was collected into 1.5-ml microcentrifuge tubes by centrifugation at 3000*g* for 3 min. The cell pellets were embedded in 15 μl of collagen gel (2 mg/ml; Advanced BioMatrix, catalog no. 5005), and the mixture was centrifuged again at 3000*g* for 3 min to facilitate embedding. The microcentrifuge tubes were incubated at 37°C with 5% CO_2 for 40 min to solidify the collagen gel. Afterward, the collagen gel–embedded cell pellets were transferred into No LIF medium and cultured overnight in 24-well plates pretreated with 2% (w/v) Poly-HEMA. The next day, the cell pellets isolated from collagen gel were then transplanted into the left renal capsule of the 8-week-old male C57BL/6JGpt mice (#N000013, GemPharmatech Co. Ltd., Chengdu, China), with up to three samples transplanted per mouse. All grafts were collected 3 to 5 weeks posttransplantation, fixed in 4% PFA, and processed for further analysis.

Mouse mandibular defect model

A total of 1.5×10^5 sorted day-16 *Msx1*$^+$ or *Msx1*$^-$ cells was collected into 1.5-ml microcentrifuge tubes by centrifugation at 300*g* for 5 min and resuspended in 8 μl of 7.5% gelatin methacryloyl (GelMA; Engineering For Life, catalog no. EFLGM-90). After anesthesia and surgical exposure of the mandible, a full-thickness penetrating defect with a diameter of 1.6 mm was created using a dental bur in the 8-week-old male C57BL/6JGpt mice. The defect site was cleaned with PBS, filled with 8 μl of the cell suspension, and cross-linked by ultraviolet irradiation for 15 s. Mandibles were harvested 5 weeks after surgery and fixed in 4% PFA for subsequent analysis.

Frozen section and histological evaluations of tissues

Mouse embryos, graft samples, and mandibles were fixed in 4% PFA at 4°C overnight, followed by decalcification in 10% (w/v) EDTA (Solarbio, catalog no. E8040) at RT for 2 days. Samples were then dehydrated in 15% and subsequently 30% (w/v) sucrose until they sank, incubated in a 1:1 mixture of 30% sucrose and Optimal Cutting Temperature (OCT) compound (Sakura, catalog no. 4583) for 1 hour, and lastly embedded in OCT. Embedded blocks were flash frozen at −80°C for 24 hours to optimize cutting consistency. Cryosectioning was performed using a refrigerated microtome (Leica, CM1950) at 6-μm thickness, with sections stored at −20°C until further analysis. For histological staining, sections were rehydrated in PBS for 10 min to remove residual OCT, followed by Alcian Blue, Masson's trichrome, or hematoxylin and eosin (H&E) staining. Alcian Blue staining was performed as previously described, except that PBS washing was replaced with rinsing in ultrapure water, followed by rapid dehydration in 95 and 100% ethanol for 1 min each. H&E (Solarbio, catalog no. G1120) and Masson's trichrome (Solarbio, catalog no. G1346) staining were performed according to the manufacturer's instructions. All sections were cleared in xylene and mounted with neutral resin. Bright-field images were captured using a digital slide scanner (WISLEAP, WS-10).

μCT analysis

The 5-week grafts were scanned using a μCT50 system (SCANCO Medical, Bassersdorf, Switzerland) at a spatial resolution of 5 μm (70 kilovolt peak, 200 μA, and 300-ms integration time). Three-dimensional (3D) imaging reconstruction was performed using the system's software, with the region of interest defined by a threshold range of 220 to 1000.

The mandibles from the defect model were scanned using a SkyScan 1176 μCT system (Bruker, Billerica, MA, USA) at a spatial resolution of 9 μm (60 kV and 400 μA). 3D reconstructions were performed using NRecon (v 1.6.9), and quantitative analyses of bone volume fraction (BV/TV), trabecular separation (Tb.Sp), and trabecular number (Tb.N) at the defect sites were carried out using CTAn (v 1.14.10.0).

Immunofluorescence staining

For immunofluorescence staining, frozen sections were rehydrated in PBS for 5 min to remove residual OCT compound. Meanwhile, mESCs were cultured in No LIF medium supplemented with Dox (1 μg/ml) on glass-bottom culture dishes (NEST, catalog no. 801001) for 2 days and then fixed in 4% PFA for 15 min at RT, followed by three PBS washes. For intracellular antigen detection, both sections and cells were permeabilized with 0.3% (v/v) Triton X-100 (Sigma-Aldrich, catalog no. T9284) for 5 min and rinsed with PBS. Samples were then incubated with blocking buffer [5% (w/v) BSA in PBS] at RT for 1 hour before overnight incubation at 4°C with primary antibodies diluted in blocking buffer. After washing, secondary antibodies were stained at RT for 1 hour in the dark. Filamentous actin (F-actin) was labeled using Actin-Tracker Near-IR-680 (Beyotime, catalog no. C2211S) according to the manufacturer's instructions. Nuclei were counterstained using 4′,6-diamidino-2-phenylindole (DAPI) mounting medium (Thermo Fisher Scientific, catalog no. D1306) after final PBS washes. Imaging of tissue sections was performed with an Olympus VS200 slide scanner, while cell imaging was conducted using confocal microscopes (Olympus SpinFV-COMB and Zeiss LSM 980). Day-2 *Dlx2*-OE EBs were fixed with 4% PFA and 0.05% glutaraldehyde, cleared, and immunostained according to the previously published protocol (*76*). All the antibodies were listed in table S2.

Transcriptome analysis by bulk RNA-seq

Total RNAs were extracted from mESCs, day-2 *Dlx2*-OE EBs, day-2 GFP-OE EBs, day-8 *Msx1*$^+$ and *Msx1*$^-$ cells, and day-16 *Msx1*$^+$ and *Msx1*$^-$ cells ($n = 2$ per group). Sequencing libraries were prepared after adapter removal and quality trimming of raw reads. The clean reads were mapped against the mouse genome (*Mus musculus*, GRCm38) using HISAT2 (v 2.1.0). The expression level of each gene was quantified guided by reference annotation (*M. musculus*, GRCm38.91) using featureCounts (v 1.6.0). DEG analysis was performed using the DESeq2 1.18.1 package in R3.4.3, and DEGs were called by false discovery rate < 0.05 and fold change (FC) > 2. GO enrichment analysis was performed using the clusterProfiler

package. Significant pathways were identified on the basis of the Kyoto Encyclopedia of Genes and Genomes. Bulk RNA-seq data have been submitted to the Gene Expression Omnibus (GEO) database (GSE297346)

Quantitative PCR

Total RNAs were extracted from cells using TRI Reagent (Sigma-Aldrich, catalog no. T9424), and reverse transcription was performed with the PrimeScript RT reagent kit with gDNA Eraser (Takara, catalog no. RR047A) following the manufacturer's instructions. qPCR was conducted on a CFX384 Optics Module (Bio-Rad, USA) using AceQ Universal SYBR qPCR Master Mix (Vazyme, catalog no. Q511-02). Relative mRNA expression was calculated using the comparative threshold cycle ($\Delta\Delta C_t$) method. Primer sequences were listed in table S3.

10x Genomics scRNA-seq

Dlx2-OE EB formation and culture were performed as previously described. EBs collected at four time points (days 2, 8, 12, and 16) were dissociated into single-cell suspensions as detailed in the "Flow cytometry" section. Following centrifugation at 450*g* for 3 min, cells were washed once with No LIF medium and resuspended in DMEM containing 10% (v/v) FBS. The suspensions were filtered twice with a 70-μm strainer. Cell number and viability were assessed using the Countess II Automated Cell Counter (Thermo Fisher Scientific, catalog no. AMQAX1000). The resulting single-cell suspensions were subjected to scRNA-seq using the 10x Genomics platform. Library preparation and sequencing were performed by HaploX Co. Ltd. (Shenzhen).

Processing of scRNA-seq raw data

The scRNA-seq raw data were processed using CellRanger software (v 7.1.0) from the 10x Genomics website (www.10xgenomics.com/software). Sequencing reads from each sample were aligned to the GRCm38 reference genome using the CellRanger count module to perform sequence alignment, quality filtering, barcode and unique molecular identifier (UMI) counting, and generating of filtered feature-barcode matrices. The scRNA-seq data have been deposited to the GEO database (GSE297347).

Data integration, reduction, visualization, and cell type annotation

The matrices were subsequently processed using the Seurat R package (v 4.3.0.1) (*77*). All samples were initially merged into a single Seurat object with unique sample names stored in "orig.ident" of metadata. Further quality control was applied to filter out low-quality cells using thresholds of (i) <1000 detected genes and (ii) >10% mitochondrial gene counts. To optimize computational efficiency, we performed random subsampling of 5000 cells per sample before downstream analyses. The filtered gene expression matrix was normalized using NormalizeData function with default parameters, followed by identification of the top 2000 highly variable genes (HVGs). Cell cycle phase assignment was performed via the CellCycleScoring function, with subsequent regression of cell cycle effects. Principal components analysis (PCA) was conducted on scaled HVG expression data, where the top 20 PCs, capturing ≥80% cumulative variance, was selected on the basis of elbow plot evaluation of 30 initial PCs. These PCs were then used for batch correction using Harmony (v 0.1.1) (*78*) integration with default parameters. The clustering resolutions across a range of 0.2 to 1.2 (step size = 0.1) were systematically evaluated using the FindNeighbors and FindClusters functions, and the hierarchical relationships between clusters were visualized using the clustree R package (v 0.5.0) (*79*), with a final resolution of 0.4 selected on the basis of dendrogram plot. The cluster-specific marker genes were identified using the FindAllMarkers function and annotated key cell populations, including ESCs, neural tube cells, neural crest cells, ectomesenchymal cells, VSMCs, and skeletogenic progenitors based on canonical markers. Continuous developmental state transitions were reconstructed by performing diffusion map analysis using the destiny R package (v 3.22.0) (*80*) with default parameters on Harmony-corrected embeddings (50 dimensions), followed by visualization via t-distributed stochastic neighbor embedding (t-SNE; perplexity = 150) using the full diffusion component space.

Pseudotime inference and lineage selection

A single ESC ("day2_TAGCACACATCCCACT-1") was selected as the trajectory origins using CellSelector function. Pseudotime analysis was performed with Palantir (v 1.3.3) (*81*) by first computing diffusion maps with default parameters, followed by construction of a multiscale diffusion space to resolve transcriptional relationships across hierarchies. Pseudotime trajectories were reconstructed from predefined starting cells using the palantir.core.run_palantir function, generating two key metrics: (i) pseudotime values ordering cells along developmental progression and (ii) entropy measurements quantifying single-cell differentiation potential. Both metrics were subsequently integrated into Seurat object's metadata for downstream analysis. For developmental trajectory analysis, we used Slingshot (v 2.4.0) (*82*) with ESCs designated as trajectory origins to generate smoothed principal curves representing differentiation pathways.

Identification and visualization of dynamic features

Dynamic gene expression patterns were resolved by applying the MAGIC (Markov affinity-based graph imputation of cells) algorithm (v 2.0.3) (*83*) to genes detected in at least 50 cells for noise reduction and profile smoothing. The skeletogenesis lineage was then isolated as a Seurat subset object. Subsequent analyses were conducted using the Single-Cell Pipeline (SCP) package (v 0.4.8), with the RunDynamicFeatures function invoked using "n_candidates = 750." These features were subjected to dynamic heatmap visualization in conjunction with Gene Ontology Biological Process (GO_BP) enrichment analysis to identify functionally significant expression trends. Last, the DynamicPlot function was executed to visualize stage-specific marker dynamics along pseudotime, providing temporal resolution of the differentiation trajectory.

RNA velocity

RNA velocity analysis was performed using Velocyto (v 0.17.17) (*84*) to quantify spliced and unspliced transcripts, followed by processing with scVelo (v 0.3.2) (*85*). Genes were filtered and normalized using the scv.pp.filter_and_normalize function with default parameters. Velocity estimation was conducted by scvelo.tl.velocity function in steady-state mode, with results visualized as streamlines on t-SNE embeddings using scvelo.tl.velocity_graph and scvelo.pl.velocity_embedding_stream functions.

AlphaFold structure prediction

The predicted 3D structure of DLX2-LAP2α complex was generated using AlphaFold 3 with multimer settings (*44*), executed on the National Institutes of Health High-Performance Computing Biowulf cluster. The resulting models were visualized using PyMOL (Open-Source, v 3.1).

Immunoprecipitation

For co-IP, day-2 EBs and facial prominences of E10.5 embryos were collected and washed three times with PBS. Total proteins were

extracted using NP-40 lysis buffer (Beyotime, catalog no. P0013F) supplemented with a protease inhibitor cocktail (MedChemExpress, catalog no. HY-K0010), incubated on ice for 30 min, and centrifuged at 12,000*g* for 30 min at 4°C. Protein concentrations were quantified by bicinchoninic acid (BCA) assay (Thermo Fisher Scientific, catalog no. A65453), and 700 μg of protein per sample was diluted to 500 μl. After preclearing with magnetic beads, the lysates were incubated overnight at 4°C with anti-FLAG, anti-pan LAP2, anti-H3K27ac, or control IgG antibodies, followed by a 4-hour incubation with Protein G or Protein A/G magnetic beads (Invitrogen, catalog no. 10004D; MedChemExpress, catalog no. HY-K0202). Immune complexes were collected using a magnetic stand and washed three times with NP-40 lysis buffer. For western blotting, beads were resuspended in 50 μl per sample 2× SDS–polyacrylamide gel electrophoresis (SDS-PAGE) loading buffer (Solarbio, catalog no. P1040), denatured at 95°C for 10 min. After removing beads, samples were stored at −80°C until use. For mass spectrometry analysis, the beads were further washed three times with PBS before protein elution. To release histone complexes and degrade DNA, EtBr (27 μg/ml; Thermo Fisher Scientific, catalog no. 15585011) and Benzonase (50 U/ml; Sigma-Aldrich, catalog no. E8263-5KU) were added to the cell lysates after centrifugation, followed by incubation on ice for 30 min and an additional centrifugation for 30 min. The resulting supernatants were then used for co-IP.

Western blotting

Samples containing 10 μg of total protein or 10 μl of immunoprecipitated proteins were separated by SDS-PAGE and transferred onto 0.2- or 0.45-μm polyvinylidene difluoride membranes (Millipore, catalog nos. ISEQ00010 and IPVH00010) using a Bio-Rad SD Semi-Dry Electrophoretic Transfer Cell. Membranes were blocked in 5% (w/v) nonfat milk (Sangon, catalog no. A600669-0250) in Tris-buffered saline with Tween 20 (TBS/T) for 1 hour at RT and incubated overnight at 4°C with primary antibodies diluted in 5% (w/v) BSA in TBS/T. After three 5-min washes in TBS/T, membranes were incubated with secondary antibodies diluted in blocking buffer for 1 hour at RT. Following another three washes in TBS/T, signals were developed using ECL Western Blotting Substrate (Affinity, catalog no. KF8005) and imaged with a Bio-Rad Chemi Doc Imaging System. For loading control detection, membranes were incubated with horseradish peroxidase–conjugated anti–glyceraldehyde-3-phosphate dehydrogenase (GAPDH) antibody (HUABIO, catalog no. ET1702-66) in blocking buffer for 1 hour at RT and washed before imaging. Antibodies used were listed in table S2.

Liquid chromatography–mass spectrometry

Immunoprecipitated proteins were eluted from magnetic beads using a lysis buffer containing 6 M urea and 2 M thiourea in 100 mM ammonium bicarbonate, supplemented with 20 mM Tris (2-carboxyethyl) phosphine and 40 mM iodoacetamide for simultaneous protein extraction, reduction, and alkylation. Pressure cycling technology (PCT) was applied at 45 kpsi (310.26 MPa) for 30 s with 10-s intervals at 30°C for 90 cycles. For digestion, 5 μg of trypsin and 1 μg of Lys-C were added at enzyme-to-protein ratios of 1:50 and 1:80, respectively, followed by PCT at 20 kpsi (137.9 MPa) for 50 s with 10-s intervals at 30°C for 120 cycles. The resulting peptides were desalted using C18 cartridges and vacuum dried.

Liquid chromatography–mass spectrometry (LC-MS) procedures were performed as previously described (*86*). Briefly, proteins were resolved in 0.1% formic acid (FA) and analyzed using an EASY-nLC 1200 system (Thermo Fisher Scientific, USA) coupled to an Orbitrap Fusion Lumos Tribrid mass spectrometer system (Thermo Fisher Scientific, USA). Samples were loaded onto a 75 μm × 15 cm analytical column packed with 1.6-μm C18 particles (Dr. Maisch, Germany) at a flow rate of 300 nl/min. Chromatographic separated was carried out with a 120-min gradient at 55°C using 0.1% FA (solvent A) and 80% acetonitrile (ACN) with 0.1% FA (solvent B) as mobile phases: 6 to 37% B over 110 min, 37 to 100% B over 3 min, and 100% B for 7 min. At 55°C with a 120-min gradient using 0.1% FA (solvent A) and 80% ACN with 0.1% FA (solvent B): 6 to 37% solvent B in 110 min, 37 to 100% solvent B in 3 min, and 100% solvent B for 7 min. Spray voltage, ion transfer tube temperature, and other ion source settings were adjusted on the basis of instrument tuning conditions. Mass spectrometry analyses and specific parameters used here were based on a previously published study (*87*).

LC-MS data analysis

Following proteomic profiling, raw mass spectrometry data were processed to extract label-free quantification (LFQ) intensity values for each identified protein across experimental group (FLAG + Dox) and control groups (FLAG – Dox and IgG). Mean LFQ intensity was calculated for each group, and proteins with higher expression in the experimental group relative to both controls were selected. Differential expression analysis was then performed using DESeq2 (v 1.38.3) for two pairwise comparisons (FLAG + Dox versus FLAG – Dox and FLAG + Dox versus IgG). Significantly enriched proteins (SEPs) were defined by adjusted $P < 0.05$ and $\log_2 FC > 2$. The final candidate list was derived from the intersection of SEPs from both comparisons. The LC-MS data have been submitted to the PRoteomics IDEntifications (PRIDE) database (PXD064236).

CUT&Tag library preparation

CUT&Tag experiment was conducted following the established protocol (*88*, *89*). Single-cell suspensions were prepared from day-2 EBs by trypsinization, followed by cell counting and centrifugation at 600*g* for 3 min at RT. The liquid was drained, and the cells were resuspended in 4 ml of wash buffer at RT while pipetting. After centrifugation at 600*g* for 3 min at RT, the liquid was drained again. The cells were then resuspended in 1.5 ml of wash buffer and held on ice until the beads were ready. The cells were incubated with Concanavalin A–coated magnetic beads (Bangs Laboratories, catalog no. BP531). Bead-bound cells were resuspended in 50 μl of ice-cold antibody buffer, and a 1:50 dilution of the primary antibody [mouse monoclonal anti-FLAG antibody (Sigma-Aldrich, catalog no. F1804); rabbit polyclonal anti-LAP2α antibody (Abcam, catalog no. ab5162); rabbit polyclonal anti-Histone H3K9me3 (Active Motif, catalog no. 39161); rabbit polyclonal anti-Histone H3K27ac (Abcam, catalog no. ab4729); negative control antibodies: guinea pig α-rabbit IgG antibody (Antibodies Online, catalog no. ABIN101961) or rabbit anti-mouse IgG H&L (Abcam, catalog no. ab46540)] was added. The samples were incubated overnight at 4°C, and tubes were placed on a magnetic rack to remove the supernatants. Secondary antibody (rabbit anti-mouse IgG H&L (Abcam, catalog no. ab46540) or guinea pig α-rabbit IgG antibody (Antibodies Online, catalog no. ABIN101961) was added, and the samples were incubated at RT for 1 hour. After placing the tubes on the magnetic rack and removing the supernatants, pA-Tn5 transposon (incubated at RT for 1 hour and in-house prepared) was added. Tagmentation was carried out for 1 hour at 37°C, and DNA was extracted using phenol-chloroform-isoamyl alcohol (Thermo Fisher Scientific, catalog no. 15593049). Purified DNA fragments were amplified by PCR for 17 cycles, and the PCR

products were purified using VAHTS DNA Clean Beads (Vazyme, catalog no. N411) according to the manufacturer's instructions. CUT&Tag library construction was performed in duplicates or triplicates, and the libraries were sequenced at 150–base pair paired end by Berry Genomics Co., Ltd. (Beijing, China).

CUT&Tag data analysis

The CUT&Tag data analysis workflow adhered to the previously established protocol (*88*, *89*) and was guided by the step-by-step tutorial available online (*90*). Briefly, reads underwent trimming using cutadapt 4.4, incorporating the following options: -a CTGTCTCTTATACACATCT; -A CTGTCTCTTATACACATCT. Paired-end reads were aligned to the mm10 reference genome using Bowtie2 (v 2.3.5.1), incorporating the following options: --local --very-sensitive --no-mixed --no-discordant --phred33 -I 10 -X 1000. Peak calling was executed using SEACR 1.3 (*91*). All statistically significantly enriched regions, referred to as peaks, identified in CUT&Tag data were annotated to genes using the R package ChIPseeker. Enriched motifs were calculated using Homer suite (*92*). Heatmaps were produced using the computeMatrix and plotHeatmap functions in DeepTools (*93*). The CUT&Tag data have been submitted to the GEO database (GSE297345) and Sequence Read Archive database (PRJNA1354472).

Statistical analysis

All statistical analyses were performed using SPSS v27.0 (IBM, Armonk, NY, USA), with specific methods detailed in each figure legend. Data were presented as mean ± SD. Group comparisons were conducted using unpaired two-tailed Student's *t* test or one-way analysis of variance (ANOVA), followed by Dunnett's or Tukey's post hoc test. Statistical significance was defined as $^{*}P < 0.05$, $^{**}P < 0.01$, $^{***}P < 0.001$, and $^{****}P < 0.0001$.

Supplementary Materials

This PDF file includes:

Figs. S1 to S9

Tables S1 to S3

REFERENCES

1. M. L. Martik, M. E. Bronner, Riding the crest to get a head: Neural crest evolution in vertebrates. *Nat. Rev. Neurosci.* **22**, 616–626 (2021).
2. L. Selleri, F. M. Rijli, Shaping faces: Genetic and epigenetic control of craniofacial morphogenesis. *Nat. Rev. Genet.* **24**, 610–626 (2023).
3. P. Fabian, J. G. Crump, Reassessing the embryonic origin and potential of craniofacial ectomesenchyme. *Semin. Cell Dev. Biol.* **138**, 45–53 (2023).
4. E. A. Zamora, T. Ahmad, *Dandy Walker Malformation* (StatPearls Publishing, 2022).
5. M. R. Proctor, J. G. Meara, A review of the management of single-suture craniosynostosis, past, present, and future. *J. Neurosurg. Pediatr.* **24**, 622–631 (2019).
6. A. F. Goodwin, R. Kim, J. O. Bush, O. D. Klein, From bench to bedside and back: Improving diagnosis and treatment of craniofacial malformations utilizing animal models. *Curr. Top. Dev. Biol.* **115**, 459–492 (2015).
7. M. Yu, L. Ma, Y. Yuan, X. Ye, A. Montagne, J. He, T. V. Ho, Y. Wu, Z. Zhao, N. Sta Maria, R. Jacobs, M. Urata, H. Wang, B. V. Zlokovic, J. F. Chen, Y. Chai, Cranial suture regeneration mitigates skull and neurocognitive defects in craniosynostosis. *Cell* **184**, 243–256.e18 (2021).
8. A. Blentic, P. Tandon, S. Payton, J. Walshe, T. Carney, R. N. Kelsh, I. Mason, A. Graham, The emergence of ectomesenchyme. *Dev. Dyn.* **237**, 592–601 (2008).
9. L. Menendez, T. A. Yatskievych, P. B. Antin, S. Dalton, Wnt signaling and a Smad pathway blockade direct the differentiation of human pluripotent stem cells to multipotent neural crest cells. *Proc. Natl. Acad. Sci. U.S.A.* **108**, 19240–19245 (2011).
10. S. M. Chambers, Y. Qi, Y. Mica, G. Lee, X.-J. Zhang, L. Niu, J. Bilsland, L. Cao, E. Stevens, P. Whiting, Combined small-molecule inhibition accelerates developmental timing and converts human pluripotent stem cells into nociceptors. *Nat. Biotechnol.* **30**, 715–720 (2012).
11. J. O. Hackland, T. J. Frith, O. Thompson, A. M. Navarro, M. I. Garcia-Castro, C. Unger, P. W. Andrews, Top-down inhibition of BMP signaling enables robust induction of hPSCs into neural crest in fully defined, xeno-free conditions. *Stem Cell Rep.* **9**, 1043–1052 (2017).
12. J. Tchieu, B. Zimmer, F. Fattahi, S. Amin, N. Zeltner, S. Chen, L. Studer, A modular platform for differentiation of human PSCs into all major ectodermal lineages. *Cell Stem Cell* **21**, 399-410. e397 (2017).
13. K. Umeda, H. Oda, Q. Yan, N. Matthias, J. Zhao, B. R. Davis, N. Nakayama, Long-term expandable SOX9+ chondrogenic ectomesenchymal cells from human pluripotent stem cells. *Stem Cell Rep.* **4**, 712–726 (2015).
14. J. Huang, K. P. U, F. Yang, Z. Ji, J. Lin, Z. Weng, L. L. Tsang, T. D. Merson, Y. C. Ruan, C. Wan, G. Li, X. Jiang, Human pluripotent stem cell-derived ectomesenchymal stromal cells promote more robust functional recovery than umbilical cord-derived mesenchymal stromal cells after hypoxic-ischaemic brain damage. *Theranostics* **12**, 143–166 (2022).
15. M. Jamal, S. L. Lewandowski, M. L. Lawton, G. T. Huang, L. Ikonomou, Derivation and characterization of putative craniofacial mesenchymal progenitor cells from human induced pluripotent stem cells. *Stem Cell Res.* **33**, 100–109 (2018).
16. J. L. Rubenstein, A. S. Nord, M. Ekker, DLX genes and proteins in mammalian forebrain development. *Development* **151**, dev202684 (2024).
17. M. J. Depew, C. A. Simpson, M. Morasso, J. L. Rubenstein, Reassessing the Dlx code: The genetic regulation of branchial arch skeletal pattern and development. *J. Anat.* **207**, 501–561 (2005).
18. H. Hu, Y. Duan, K. Wang, H. Fu, Y. Liao, T. Wang, Z. Zhang, F. Kang, B. Zhang, H. Zhang, F. Huo, Y. Yin, G. Chen, H. Hu, H. Cai, W. Tian, Z. Li, Dental niche cells directly contribute to tooth reconstitution and morphogenesis. *Cell Rep.* **41**, 111737 (2022).
19. P. He, B. A. Williams, D. Trout, G. K. Marinov, H. Amrhein, L. Berghella, S. T. Goh, I. Plajzer-Frick, V. Afzal, L. A. Pennacchio, D. E. Dickel, A. Visel, B. Ren, R. C. Hardison, Y. Zhang, B. J. Wold, The changing mouse embryo transcriptome at whole tissue and single-cell resolution. *Nature* **583**, 760–767 (2020).
20. H. Wang, Y. Yang, J. Liu, L. Qian, Direct cell reprogramming: Approaches, mechanisms and progress. *Nat. Rev. Mol. Cell Biol.* **22**, 410–424 (2021).
21. I. Satokata, R. Maas, Msx1 deficient mice exhibit cleft palate and abnormalities of craniofacial and tooth development. *Nat. Genet.* **6**, 348–356 (1994).
22. M. Ishii, J. Han, H. Y. Yen, H. M. Sucov, Y. Chai, R. E. Maxson Jr., Combined deficiencies of Msx1 and Msx2 cause impaired patterning and survival of the cranial neural crest. *Development* **132**, 4937–4950 (2005).
23. A. H. Monsoro-Burq, PAX transcription factors in neural crest development. *Semin. Cell Dev. Biol.* **44**, 87–96 (2015).
24. M. Takechi, N. Adachi, T. Hirai, S. Kuratani, S. Kuraku, The Dlx genes as clues to vertebrate genomics and craniofacial evolution. *Semin. Cell Dev. Biol.* **24**, 110–118 (2013).
25. J. O. Bush, R. Jiang, Palatogenesis: Morphogenetic and molecular mechanisms of secondary palate development. *Development* **139**, 231–243 (2012).
26. J. Laurikkala, M. Mikkola, T. Mustonen, T. Aberg, P. Koppinen, J. Pispa, P. Nieminen, J. Galceran, R. Grosschedl, I. Thesleff, TNF signaling via the ligand-receptor pair ectodysplasin and edar controls the function of epithelial signaling centers and is regulated by Wnt and activin during tooth organogenesis. *Dev. Biol.* **229**, 443–455 (2001).
27. T. Ishitani, K. Matsumoto, A. B. Chitnis, M. Itoh, Nrarp functions to modulate neural-crest-cell differentiation by regulating LEF1 protein stability. *Nat. Cell Biol.* **7**, 1106–1112 (2005).
28. Y. Zhao, Y. J. Guo, A. C. Tomac, N. R. Taylor, A. Grinberg, E. J. Lee, S. Huang, H. Westphal, Isolated cleft palate in mice with a targeted mutation of the LIM homeobox gene lhx8. *Proc. Natl. Acad. Sci. U.S.A.* **96**, 15002–15006 (1999).
29. D. ten Berge, A. Brouwer, J. Korving, J. F. Martin, F. Meijlink, Prx1 and Prx2 in skeletogenesis: Roles in the craniofacial region, inner ear and limbs. *Development* **125**, 3831–3842 (1998).
30. T. Yoshida, P. Vivatbutsiri, G. Morriss-Kay, Y. Saga, S. Iseki, Cell lineage in mammalian craniofacial mesenchyme. *Mech. Dev.* **125**, 797–808 (2008).
31. D. Doro, A. Liu, J. S. Lau, A. K. Rajendran, C. Healy, M. Krstic, A. E. Grigoriadis, S. Iseki, K. J. Liu, Cranial suture lineage and contributions to repair of the mouse skull. *Development* **151**, dev202116 (2024).
32. B. Behr, M. T. Longaker, N. Quarto, Differential activation of canonical Wnt signaling determines cranial sutures fate: A novel mechanism for sagittal suture craniosynostosis. *Dev. Biol.* **344**, 922–940 (2010).
33. Y. Chai, R. E. Maxson Jr., Recent advances in craniofacial morphogenesis. *Dev. Dyn.* **235**, 2353–2375 (2006).
34. R. Soldatov, M. Kaucka, M. E. Kastriti, J. Petersen, T. Chontorotzea, L. Englmaier, N. Akkuratova, Y. Yang, M. Häring, V. Dyachuk, C. Bock, M. Farlik, M. L. Piacentino, F. Boismoreau, M. M. Hilscher, C. Yokota, X. Qian, M. Nilsson, M. E. Bronner, L. Croci, W. Y. Hsiao, D. A. Guertin, J. F. Brunet, G. G. Consalez, P. Ernfors, K. Fried, P. V. Kharchenko, I. Adameyko, Spatiotemporal structure of cell fate decisions in murine neural crest. *Science* **364**, eaas9536 (2019).
35. B. Li, S. Kuriyama, M. Moreno, R. Mayor, The posteriorizing gene Gbx2 is a direct target of Wnt signalling and the earliest factor in neural crest induction. *Development* **136**, 3267–3278 (2009).
36. M. Simões-Costa, M. E. Bronner, Establishing neural crest identity: A gene regulatory recipe. *Development* **142**, 242–257 (2015).

37. M. Minoux, S. Holwerda, A. Vitobello, T. Kitazawa, H. Kohler, M. B. Stadler, F. M. Rijli, Gene bivalency at Polycomb domains regulates cranial neural crest positional identity. *Science* **355**, eaal2913 (2017).
38. H. Bildsoe, D. A. Loebel, V. J. Jones, Y.-T. Chen, R. R. Behringer, P. P. Tam, Requirement for Twist1 in frontonasal and skull vault development in the mouse embryo. *Dev. Biol.* **331**, 176–188 (2009).
39. J. W. Vincentz, B. A. Firulli, A. Lin, D. B. Spicer, M. J. Howard, A. B. Firulli, Twist1 controls a cell-specification switch governing cell fate decisions within the cardiac neural crest. *PLOS Genet.* **9**, e1003405 (2013).
40. G. L. Basatemur, H. F. Jørgensen, M. C. Clarke, M. R. Bennett, Z. Mallat, Vascular smooth muscle cells in atherosclerosis. *Nat. Rev. Cardiol.* **16**, 727–744 (2019).
41. G. K. Owens, M. S. Kumar, B. R. Wamhoff, Molecular regulation of vascular smooth muscle cell differentiation in development and disease. *Physiol. Rev.* **84**, 767–801 (2004).
42. M. Cai, Y. Huang, R. Ghirlando, K. L. Wilson, R. Craigie, G. M. Clore, Solution structure of the constant region of nuclear envelope protein LAP2 reveals two LEM-domain structures: One binds BAF and the other binds DNA. *EMBO J.* **20**, 4399–4407 (2001).
43. A. N. Mirza, S. A. McKellar, N. M. Urman, A. S. Brown, T. Hollmig, S. Z. Aasi, A. E. Oro, LAP2 proteins chaperone GLI1 movement between the lamina and chromatin to regulate transcription. *Cell* **176**, 198–212.e15 (2019).
44. J. Abramson, J. Adler, J. Dunger, R. Evans, T. Green, A. Pritzel, O. Ronneberger, L. Willmore, A. J. Ballard, J. Bambrick, Accurate structure prediction of biomolecular interactions with AlphaFold 3. *Nature* **630**, 493–500 (2024).
45. C. T. McMurray, K. Van Holde, Binding of ethidium bromide causes dissociation of the nucleosome core particle. *Proc. Natl. Acad. Sci. U.S.A.* **83**, 8472–8476 (1986).
46. M. Foltman, C. Evrin, G. De Piccoli, R. C. Jones, R. D. Edmondson, Y. Katou, R. Nakato, K. Shirahige, K. Labib, Eukaryotic replisome components cooperate to process histones during chromosome replication. *Cell Rep.* **3**, 892–904 (2013).
47. D. Theofilatos, T. Ho, G. Waitt, T. Äijö, L. M. Schiapparelli, E. J. Soderblom, A. Tsagaratou, Deciphering the TET3 interactome in primary thymic developing T cells. *Iscience* **27**, 109782 (2024).
48. D. Ji, C. Shao, J. Yu, Y. Hou, X. Gao, Y. Wu, L. Wang, P. Chen, FOXA1 forms biomolecular condensates that unpack condensed chromatin to function as a pioneer factor. *Mol. Cell* **84**, 244–260.e7 (2024).
49. L. Tao, Y. Zhou, Y. Luo, J. Qiu, Y. Xiao, J. Zou, Y. Zhang, X. Liu, X. Yang, K. Gou, J. Xu, X. Guan, X. Cen, Y. Zhao, Epigenetic regulation in cancer therapy: From mechanisms to clinical advances. *MedComm Oncol.* **3**, e59 (2024).
50. É. Heude, K. Bouhali, Y. Kurihara, H. Kurihara, G. Couly, P. Janvier, G. Levi, Jaw muscularization requires Dlx expression by cranial neural crest cells. *Proc. Natl. Acad. Sci. U.S.A.* **107**, 11441–11446 (2010).
51. E. W. Brunskill, A. S. Potter, A. Distasio, P. Dexheimer, A. Plassard, B. J. Aronow, S. S. Potter, A gene expression atlas of early craniofacial development. *Dev. Biol.* **391**, 133–146 (2014).
52. R. F. Robledo, L. Rajan, X. Li, T. Lufkin, The Dlx5 and Dlx6 homeobox genes are essential for craniofacial, axial, and appendicular skeletal development. *Genes Dev.* **16**, 1089–1101 (2002).
53. M. P. Verzi, P. Agarwal, C. Brown, D. J. McCulley, J. J. Schwarz, B. L. Black, The transcription factor MEF2C is required for craniofacial development. *Dev. Cell* **12**, 645–652 (2007).
54. N. Adhikari, Z. Wu, Y. Huang, Y. Lan, R. Jiang, Twist1 acts upstream of the Dlx5-Hand2 pathway to pattern the mammalian jaw. *J. Dent. Res.* **104**, 310–319 (2025).
55. S. Alappat, Z. Y. Zhang, Y. P. Chen, Msx homeobox gene family and craniofacial development. *Cell Res.* **13**, 429–442 (2003).
56. J. Han, M. Ishii, P. Bringas Jr., R. L. Maas, R. E. Maxson Jr., Y. Chai, Concerted action of Msx1 and Msx2 in regulating cranial neural crest cell differentiation during frontal bone development. *Mech. Dev.* **124**, 729–745 (2007).
57. I. Satokata, L. Ma, H. Ohshima, M. Bei, I. Woo, K. Nishizawa, T. Maeda, Y. Takano, M. Uchiyama, S. Heaney, Msx2 deficiency in mice causes pleiotropic defects in bone growth and ectodermal organ formation. *Nat. Genet.* **24**, 391–395 (2000).
58. S. Guo, Y. Zhang, T. Zhou, D. Wang, Y. Weng, Q. Chen, J. Ma, Y. Li, L. Wang, GATA4 as a novel regulator involved in the development of the neural crest and craniofacial skeleton via Barx1. *Cell Death Differ.* **25**, 1996–2009 (2018).
59. N. Pilon, D. Raiwet, R. S. Viger, D. W. Silversides, Novel pre-and post-gastrulation expression of Gata4 within cells of the inner cell mass and migratory neural crest cells. *Dev. Dyn.* **237**, 1133–1143 (2008).
60. M. O. Lee, J. Li, B. W. Davis, S. Upadhyay, H. M. Al Muhisen, L. J. Suva, T. M. Clement, L. Andersson, Hmga2 deficiency is associated with allometric growth retardation, infertility, and behavioral abnormalities in mice. *G3* **12**, jkab417 (2022).
61. S. Macrì, L. Simula, I. Pellarin, S. Pegoraro, M. Onorati, R. Sgarra, G. Manfioletti, R. Vignali, Hmga2 is required for neural crest cell specification in Xenopus laevis. *Dev. Biol.* **411**, 25–37 (2016).
62. R. Vignali, S. Marracci, HMGA genes and proteins in development and evolution. *Int. J. Mol. Sci.* **21**, 654 (2020).
63. D. M. Roth, F. Bayona, P. Baddam, D. Graf, Craniofacial development: Neural crest in molecular embryology. *Head Neck Pathol.* **15**, 1–15 (2021).
64. J. T. Jacob, R. R. Nair, B. G. Poll, C. M. Pineda, R. P. Hobbs, M. J. Matunis, P. A. Coulombe, Keratin 17 regulates nuclear morphology and chromatin organization. *J. Cell Sci.* **133**, jcs254094 (2020).
65. M. Bei, R. Maas, FGFs and BMP4 induce both Msx1-independent and Msx1-dependent signaling pathways in early tooth development. *Development* **125**, 4325–4333 (1998).
66. A. E. Coudert, L. Pibouin, B. Vi-Fane, B. L. Thomas, M. Macdougall, A. Choudhury, B. Robert, P. T. Sharpe, A. Berdal, F. Lezot, Expression and regulation of the Msx1 natural antisense transcript during development. *Nucleic Acids Res.* **33**, 5208–5218 (2005).
67. M. Bei, K. Kratochwil, R. L. Maas, BMP4 rescues a non-cell-autonomous function of Msx1 in tooth development. *Development* **127**, 4711–4718 (2000).
68. J. Sun, N. Ha, Z. Liu, Q. Bian, X. Wang, A neural crest-specific overexpression mouse model reveals the transcriptional regulatory effects of Dlx2 during maxillary process development. *Front. Physiol.* **13**, 855959 (2022).
69. J. Dai, Y. Kuang, B. Fang, H. Gong, S. Lu, Z. Mou, H. Sun, Y. Dong, J. Lu, W. Zhang, J. Zhang, Z. Wang, X. Wang, G. Shen, The effect of overexpression of Dlx2 on the migration, proliferation and osteogenic differentiation of cranial neural crest stem cells. *Biomaterials* **34**, 1898–1910 (2013).
70. S. J. McKeown, D. F. Newgreen, P. G. Farlie, Dlx2 over-expression regulates cell adhesion and mesenchymal condensation in ectomesenchyme. *Dev. Biol.* **281**, 22–37 (2005).
71. J. Jeong, J. Cesario, Y. Zhao, L. Burns, H. Westphal, J. L. Rubenstein, Cleft palate defect of Dlx1/2$^{-/-}$ mutant mice is caused by lack of vertical outgrowth in the posterior palate. *Dev. Dyn.* **241**, 1757–1769 (2012).
72. M. Qiu, A. Bulfone, I. Ghattas, J. J. Meneses, L. Christensen, P. T. Sharpe, R. Presley, R. A. Pedersen, J. L. Rubenstein, Role of the Dlx homeobox genes in proximodistal patterning of the branchial arches: Mutations of Dlx-1, Dlx-2, and Dlx-1 and -2 alter morphogenesis of proximal skeletal and soft tissue structures derived from the first and second arches. *Dev. Biol.* **185**, 165–184 (1997).
73. R. Baldock, J. Bard, D. Davidson, G. Morriss-Kay, *Kaufman's Atlas of Mouse Development Supplement: With Coronal Sections* (Academic Press, 2015).
74. A. Czechanski, C. Byers, I. Greenstein, N. Schrode, L. R. Donahue, A.-K. Hadjantonakis, L. G. Reinholdt, Derivation and characterization of mouse embryonic stem cells from permissive and nonpermissive strains. *Nat. Protoc.* **9**, 559–574 (2014).
75. D. E. Root, N. Hacohen, W. C. Hahn, E. S. Lander, D. M. Sabatini, Genome-scale loss-of-function screening with a lentiviral RNAi library. *Nat. Methods* **3**, 715–719 (2006).
76. L. Biswas, J. Chen, J. De Angelis, A. Singh, C. Owen-Woods, Z. Ding, J. M. Pujol, N. Kumar, F. Zeng, S. K. Ramasamy, Lymphatic vessels in bone support regeneration after injury. *Cell* **186**, 382–397.e324 (2023).
77. T. Stuart, A. Butler, P. Hoffman, C. Hafemeister, E. Papalexi, W. M. Mauck, Y. Hao, M. Stoeckius, P. Smibert, R. Satija, Comprehensive integration of single-cell data. *Cell* **177**, 1888–1902.e1821 (2019).
78. I. Korsunsky, N. Millard, J. Fan, K. Slowikowski, F. Zhang, K. Wei, Y. Baglaenko, M. Brenner, P. Loh, S. Raychaudhuri, Fast, sensitive and accurate integration of single-cell data with Harmony. *Nat. Methods* **16**, 1289–1296 (2019).
79. L. Zappia, A. Oshlack, Clustering trees: A visualization for evaluating clusterings at multiple resolutions. *Gigascience* **7**, giy083 (2018).
80. P. Angerer, L. Haghverdi, M. Büttner, F. J. Theis, C. Marr, F. Buettner, destiny: Diffusion maps for large-scale single-cell data in R. *Bioinformatics* **32**, 1241–1243 (2016).
81. M. Setty, V. Kiseliovas, J. Levine, A. Gayoso, L. Mazutis, D. Pe'Er, Characterization of cell fate probabilities in single-cell data with Palantir. *Nat. Biotechnol.* **37**, 451–460 (2019).
82. K. Street, D. Risso, R. B. Fletcher, D. Das, J. Ngai, N. Yosef, E. Purdom, S. Dudoit, Slingshot: Cell lineage and pseudotime inference for single-cell transcriptomics. *BMC Genomics* **19**, 1–16 (2018).
83. D. Van Dijk, R. Sharma, J. Nainys, K. Yim, P. Kathail, A. J. Carr, C. Burdziak, K. R. Moon, C. L. Chaffer, D. Pattabiraman, Recovering gene interactions from single-cell data using data diffusion. *Cell* **174**, 716–729.e727 (2018).
84. G. La Manno, R. Soldatov, A. Zeisel, E. Braun, H. Hochgerner, V. Petukhov, K. Lidschreiber, M. E. Kastriti, P. Lönnerberg, A. Furlan, RNA velocity of single cells. *Nature* **560**, 494–498 (2018).
85. V. Bergen, M. Lange, S. Peidli, F. A. Wolf, F. J. Theis, Generalizing RNA velocity to transient cell states through dynamical modeling. *Nat. Biotechnol.* **38**, 1408–1414 (2020).
86. Y. Zhong, F. Yang, T. Su, X. Wu, W. Zheng, L. Zhang, G. Liang, L. Wang, L. Wang, S. Wang, H. Yang, Proteome and phosphoproteome profiling of non-small cell lung cancer cell line A549 treated with TRAIL. *Proteomics* **23**, e2200248 (2023).
87. E. Gao, W. Li, C. Wu, W. Shao, Y. Di, Y. Liu, Data-independent acquisition-based proteome and phosphoproteome profiling across six melanoma cell lines reveals determinants of proteotypes. *Mol. Omics* **17**, 413–425 (2021).
88. H. S. Kaya-Okur, S. J. Wu, C. A. Codomo, E. S. Pledger, T. D. Bryson, J. G. Henikoff, K. Ahmad, S. Henikoff, CUT&Tag for efficient epigenomic profiling of small samples and single cells. *Nat. Commun.* **10**, 1930 (2019).
89. H. S. Kaya-Okur, D. H. Janssens, J. G. Henikoff, K. Ahmad, S. Henikoff, Efficient low-cost chromatin profiling with CUT&Tag. *Nat. Protoc.* **15**, 3264–3283 (2020).

90. S. Henikoff, J. G. Henikoff, H. S. Kaya-Okur, K. Ahmad, Efficient chromatin accessibility mapping in situ by nucleosome-tethered tagmentation. *eLife* **9**, e63274 (2020).
91. M. P. Meers, D. Tenenbaum, S. Henikoff, Peak calling by sparse enrichment analysis for CUT&RUN chromatin profiling. *Epigenetics Chromatin* **12**, 42 (2019).
92. S. Heinz, C. Benner, N. Spann, E. Bertolino, Y. C. Lin, P. Laslo, J. X. Cheng, C. Murre, H. Singh, C. K. Glass, Simple combinations of lineage-determining transcription factors prime cis-regulatory elements required for macrophage and B cell identities. *Mol. Cell* **38**, 576–589 (2010).
93. F. Ramírez, D. P. Ryan, B. Grüning, V. Bhardwaj, F. Kilpert, A. S. Richter, S. Heyne, F. Dündar, T. Manke, deepTools2: A next generation web server for deep-sequencing data analysis. *Nucleic Acids Res.* **44**, W160–W165 (2016).

Acknowledgments: We thank the Core Facilities in the College of Life Sciences, Sichuan University, for technical assistance. We also thank Y. Wang and Y. Luo from the College of Life Sciences, Sichuan University, for anti–acetylated-lysine antibody and experimental support. **Funding:** This work was supported by the following: the National Key Research and Development Program of China 2021YFA1100601 (Z.L.); the National Key Research and Development Program of China 2022YFA1104401 (Z.L.); the National Natural Science Foundation of China U25A20745 (Z.L.); the National Natural Science Foundation of China 32471507 (Z.L.); the Major Science and Technology Projects in Yunnan Province 202302AA310038 (Z.L.); the Fundamental Research Funds for the Central Universities SCU2019D013 (Z.L.); the Fundamental Research Funds for the Central Universities SCU2025D003 (Z.L.); the National Natural Science Foundation of China 32201221 (Y.D.); the National Natural Science Foundation of China 32522029 (J.C.); the National Natural Science Foundation of China 32470853 (J.C.); the 1·3·5 project for disciplines of excellence—Clinical Research Fund 2024HXFH035 (J.C.); and the 1·3·5 project for disciplines of excellence—Clinical Research Fund ZYGD23026 (J.C.). **Author contributions:** Conceptualization: H.H., Z.Z., Y.D., H.Y., and Z.L. Methodology: Z.Z., Z.X., H.H., Y.L., and Z.L. Software: Z.X., Y.Zha., and Y.Zho. Validation: Z.Z., Y.D., and Z.L. Formal analysis: Z.Z., Z.X., H.H., Y.L., Y.J., Y.Zha., Y.Zho., and Z.L. Investigation: Z.Z., H.H., Z.X., Y.L., and Z.L. Resources: Y.J., Y.Zha., Y.Zho., J.C., H.Y., and Z.L. Data curation: H.H., Z.Z., Z.X., and Z.L. Writing—original draft: Z.L., H.H., Z.Z., Z.X., and Y.L. Writing—review and editing: Z.L., Z.Z., Z.X., Y.L., J.C., and Y.D. Visualization: H.H., Z.Z., Z.X., Y.Zha., Y.Zho., and Z.L. Supervision: Y.Y., J.C., Y.D., H.Y., and Z.L. Project administration: Z.Z., H.Y., and Z.L. Funding acquisition: Z.L., J.C., and Y.D. **Competing interests:** The authors declare that they have no competing interests. **Data and materials availability:** All data and code needed to evaluate and reproduce the results in the paper are present in the paper and/or the Supplementary Materials. High-throughput sequencing datasets generated during this study, including 10x Genomics scRNA-seq, CUT&Tag-seq, and bulk RNA-seq, have been deposited in the NCBI Gene Expression Omnibus (GEO) under accession number GSE297347 (www.ncbi.nlm.nih.gov/geo/query/acc.cgi?acc=GSE297347), GSE297345 (www.ncbi.nlm.nih.gov/geo/query/acc.cgi?acc=GSE297345), PRJNA1354472 (www.ncbi.nlm.nih.gov/sra/?term=PRJNA1354472), and GSE297346 (www.ncbi.nlm.nih.gov/geo/query/acc.cgi?acc=GSE297346). The LC-MS data have been submitted to the ProteomeXchange Consortium via PRoteomics IDEntifications (PRIDE) database under accession number PXD064236 (www.ebi.ac.uk/pride/archive/projects/PXD064236).

Submitted 26 June 2025
Accepted 12 December 2025
Published 14 January 2026
10.1126/sciadv.aea0685

ScienceAdvances

DLX2 acts as a pioneer factor and drives *Msx1*+ ectomesenchyme formation from embryonic stem cells

Ziwei Zhang, Zhiheng Xu, Hong Hu, Yao Li, Youmei Jin, Yi Zhong, Yunqiu Zhang, Yike Yin, Jing Chen, Yufeng Duan, Hao Yang, and Zhonghan Li

Sci. Adv. **12** (3), eaea0685. DOI: 10.1126/sciadv.aea0685

Science Advances (ISSN 2375-2548) is published by the American Association for the Advancement of Science. 1200 New York Avenue NW, Washington, DC 20005. The title *Science Advances* is a registered trademark of AAAS.